The host-defense peptide piscidin P1 reorganizes lipid domains in membranes and decreases activation energies in mechanosensitive ion channels

Received for publication, July 17, 2019, and in revised form, October 1, 2019 Published, Papers in Press, October 16, 2019, DOI 10.1074/jbc.RA119.010232

Fatih Comert[‡1], Alexander Greenwood[§1], Joseph Maramba[¶], Roderico Acevedo[‡], Laura Lucas[‡], Thulasi Kulasinghe[‡], Leah S. Cairns[‖], Yi Wen[**], Riqiang Fu[‡‡], Janet Hammer[§§], Jack Blazyk[§§], Sergei Sukharev[¶], Myriam L. Cotten[§2], and Mihaela Mihailescu[‡3]

From the [‡]Institute for Bioscience and Biotechnology Research, Rockville, Maryland 20850, the [§]Department of Applied Science, William and Mary, Williamsburg, Virginia 23185, the [¶]Biology Department, University of Maryland, College Park, Maryland 20742, the [‖]Department of Biochemistry and Molecular Biology, The Johns Hopkins University, Baltimore, Maryland 21205, the [**]Department of Molecular Biology and Genetics, Cornell University, Ithaca, New York 14853, the [‡‡]National High Magnetic Field Laboratory, Tallahassee, Florida 32310, and the [§§]Department of Biomedical Sciences, Ohio University, Athens, Ohio 45701

Edited by Ursula Jakob

The host-defense peptide (HDP) piscidin 1 (P1), isolated from the mast cells of striped bass, has potent activities against bacteria, viruses, fungi, and cancer cells and can also modulate the activity of membrane receptors. Given its broad pharmacological potential, here we used several approaches to better understand its interactions with multicomponent bilayers representing models of bacterial (phosphatidylethanolamine (PE)/phosphatidylglycerol) and mammalian (phosphatidylcholine/cholesterol (PC/Chol)) membranes. Using solid-state NMR, we solved the structure of P1 bound to PC/Chol and compared it with that of P3, a less potent homolog. The comparison disclosed that although both peptides are interfacially bound and α-helical, they differ in bilayer orientations and depths of insertion, and these differences depend on bilayer composition. Although Chol is thought to make mammalian membranes less susceptible to HDP-mediated destabilization, we found that Chol does not affect the permeabilization effects of P1. X-ray diffraction experiments revealed that both piscidins produce a demixing effect in PC/Chol membranes by increasing the fraction of the Chol-depleted phase. Furthermore, P1 increased the temperature required for the lamellar–to–hexagonal phase transition in PE bilayers, suggesting that it imposes positive membrane curvature. Patch-clamp measurements on the inner *Escherichia coli* membrane showed that P1 and P3, at concentrations sufficient for antimicrobial activity, substantially decrease the activating tension for bacterial mechanosensitive channels. This indicated that piscidins can cause lipid redistribution and restructuring in the microenvironment near proteins. We conclude that the mechanism of piscidin's antimicrobial activity extends beyond simple membrane destabilization, helping to rationalize its broader spectrum of pharmacological effects.

Cationic host-defense peptides (HDPs)[4] represent an interesting class of membrane-active peptides that have evolved as part of innate immunity to eradicate life-threatening pathogens while having a low incidence of bacterial resistance. The HPD piscidin P1 (FFHHIFRGIVHVGKTIHRLVTG), isolated from the mast cells of striped bass (1–3), is the most potent known member of the piscidin family. It exhibits strong antimicrobial activity against a large number of Gram-positive and -negative bacteria, including methicillin-resistant *Staphylococcus aureus* (MRSA), with minimal inhibitory concentrations (MICs) in the 1–10 μmol/liter range. Notably, P1 is one of the few HDPs known to exhibit broad-spectrum antimicrobial activity while also having anti-HIV-1 (4) and anticancer properties (5). Furthermore, it displays considerable adaptability to high-salt concentrations and changing pH conditions (1, 6).

In vivo, multiple piscidins are deployed during bacterial infections. They kill bacteria at both basic (extracellularly) and acidic (phagosomes) pH values (1, 3, 7). Thus, piscidins, collec-

This work was supported in part by National Science Foundation Grants MCB-1716608 (to M. L. C.) and 1714164 (to M. M.). The authors declare that they have no conflicts of interest with the contents of this article. The content is solely the responsibility of the authors and does not necessarily represent the official views of the National Institutes of Health.

This article contains Figs. S1–S10, Tables S1–S6, and supporting Refs. 1–4.

The atomic coordinates and structure factors (codes 6PF0 and 6PEZ) have been deposited in the Protein Data Bank (http://wwpdb.org/).

[1] Both authors contributed equally to this work

[2] To whom correspondence may be addressed. Tel.: 757-221-7428; Fax: 757-221-2050; E-mail: mcotten@wm.edu.

[3] To whom correspondence may be addressed: Institute for Bioscience and Biotechnology Research, University of Maryland, 9600 Gudelsky Dr., Rockville MD 20850. Tel.: 240-314-6123; E-mail: emihailescu@ibbr.umd.edu.

[4] The abbreviations used are: HDP, host-defense peptide; P1 and P3, piscidins 1 and 3 (antimicrobial peptides from hybrid striped bass); PC, phosphatidylcholine; PE, phosphatidylethanolamine; PG, phosphatidylglycerol; Chol, cholesterol; POPC, 1-palmitoyl-2-oleoyl-*sn*-glycero-3-phosphocholine; POPG, 1-palmitoyl-2-oleoyl-*sn*-glycero-3-phosphoglycerol; POPE, 1-palmitoyl-2-oleoyl-*sn*-glycero-3-phosphoethanolamine; DC, dipolar coupling; DOPC, dioleoyl-*sn*-glycero-3-phosphocholine; diPoPE, 1,2-dipalmitoyl-*sn*-glycero-3-phosphoethanolamine; LUV, large unilamellar vesicle; GUV, giant unilamellar vesicle; P/L, peptide to lipid molar ratio; MscL, large conductance mechanosensitive ion channel; MscS, small conductance mechanosensitive ion channel; PDB, Protein Data Bank; DSPC, 1,2-distearoyl-*sn*-glycero-3-phosphocholine; CSA, anisotropic chemical shift; DPPS, 1,2-dioleoyl-*sn*-glycero-3-phospho-L-serine; TAMRA, carboxytetramethylrhodamine; HETCOR, two-dimensional heteronuclear correlation; MIC, minimal inhibitory concentration; CL, cardiolipin; DSC, differential scanning calorimetry; T, tesla; TFE, 2,2,2-trifluoroethanol; MS, mechanosensitive.

tively or individually, demonstrate pH-resiliency despite being particularly rich in histidine (20% *versus* 2% on average in other AMPs), a residue known to be responsive to pH in the physiological range. In particular, the membrane activity of P1 is pH-resilient (8). For these reasons P1 represents a promising template for molecular therapeutics, but future developments require that we examine in greater detail the physicochemical properties that make P1 an effective antimicrobial, anticancer, and antiviral peptide.

By analogy with other HDPs, the direct cytotoxicity and antimicrobial activities of P1 are thought to derive primarily from its ability to perturb the lipid bilayer structure of cell membranes. Indeed, there is no evidence that direct bacterial killing by P1 involves binding to a specific membrane receptor site. Similar arguments have been made for other HDPs (9) as well as tarantula neurotoxins (10) because synthetic enantiomers of these peptides exhibit identical antibacterial or ion channel modulation abilities, and thus they do not display the features associated with the molecular recognition of chiral protein receptors. Interestingly, P1 exhibits strong anti-inflammatory and anesthetic properties (11), indicating that it has immunomodulatory effects on host cells. Furthermore, both P1 and its less potent piscidin homolog, P3, exclusively activate formyl peptide receptors 1 and 2 on the surface of neutrophils and induce chemotaxis through these two G-protein–coupled receptors (12). Importantly, a common denominator for these multifaceted actions of P1 is the lipid bilayer of the various bacterial, viral, and mammalian cells that the peptide recognizes and targets.

The higher specificity of cationic HDPs toward bacterial *versus* mammalian cell membranes has been broadly attributed to their electrostatic interactions with anionic lipids, such as phosphoglycerol (PG) and cardiolipin (CL), that are abundant in bacterial membranes (13–15). Conversely, it has been observed that the presence of Chol in cell membranes typically inhibits the binding and lytic activity of several HDPs (16–18). The common reasoning for this is that Chol rigidifies the bilayer and increases its hydrocarbon thickness, thereby preventing HDP insertion. However, P1 is highly active against many Chol-rich cells, such as human cancer cells (5) and HIV-1 (4). Apart from the presumed protective role of Chol to increase bilayer order and preserve the structural integrity of the membrane in the presence of HDPs, numerous studies suggest that Chol segregates within "lipid rafts," *i.e.* specialized types of membrane domains that are important for cellular function (19). Although direct detection of such domains in natural membranes is a challenge, indirect evidence of their existence and the role in protein function exists. For instance, recent investigations using super-resolution imaging showed that activation of TREK-1 channels depends on raft disruption via mechanical stress or anesthetic action in cellular membranes (20, 21). Here, we propose that, similar to other membrane-soluble anesthetic molecules and analgesic toxins (10), P1 exerts some of its actions, including its anesthetic effects (11), by causing topological changes and redistribution of liquid-ordered (L_o)–liquid-disordered (L_d) phases in membranes (22) leading to mechanical stress redistribution and modulation of membrane protein function (23).

Despite their simpler composition compared with their mammalian counterparts, bacterial cell membranes also exhibit organization in domains (24). Notably, P1 and its close homolog, P3, were found to concentrate at septal regions (25), which are known for their role in specific cellular processes (*e.g.* cell division and sporulation) and subcellular localization of membrane proteins (*e.g.* enzymes involved in the synthesis of PE, CL, and PG lipids) (24). Importantly, several studies have demonstrated that septal regions are rich in nonlamellar-forming lipids such as PE and CL (Ref. 15 and references therein). Apart from sustaining membrane proteins, these structurally-labile regions must allow extreme topological bilayer transformations, thereby rendering them particularly susceptible to the disruptive effects of HDPs.

Given that the impact of sequence variability on the interactions of P1 and P3 with mimics of bacterial cell membranes was previously addressed (8, 25, 26), this article focuses on the more membrane-active member, P1, and P3 is used for comparative purposes. With the main goal of better understanding the modes of action of P1 in heterogeneous membranes, we investigated the interactions of this peptide with a few multicomponent membrane systems, including mixtures of PC with Chol, PE with PG, as well as the natural inner cell membrane of *Escherichia coli*. We present structural and functional experimental data that reveal how P1 exploits lipid domain formation for its multifaceted action in heterogeneous membranes, including changing lipid domain distributions and ion channel activities. This new knowledge helps us better understand the broad range of P1 biological activities.

Results

Permeabilization assays of POPC/Chol vesicles in the presence of P1 and P3

Membrane permeabilization by membrane-active peptides is well-known to occur in a concentration-dependent fashion, with the threshold concentration for activity correlating with the reorientation and deeper insertion of the peptides in membranes (27–29). We prepared 1-palmitoyl-2-oleoyl-*sn*-glycero-3-phosphocholine (POPC) and 4:1 POPC/Chol large unilamellar vesicles (LUV) containing trapped calcein and measured the ability of P1 and P3 to release the fluorescent dye as a function of the peptide–to–lipid molar ratio (P/L). The assays were done at pH 7.4 when the histidine side chains are neutral (8). As shown in Fig. 1, P1 and P3 both permeabilize the two types of LUVs, and the threshold at which permeabilization occurs is characterized by a relatively high error bar compared with the other data points, presumably due to the stochastic aspects of the process that underlies leakage (30, 31). P1 is significantly more effective than P3 in both lipid systems, and the addition of Chol does not affect the effectiveness of the peptides. Indeed, the P/L producing 50% permeabilization (EC_{50}) of the POPC LUVs is lower for P1 (1:166) than P3 (1:28) and comparable within the experimental error of 20% whether POPC contains Chol or not (1:130 for P1 and 1:23 for P3). In 3:1 POPC/POPG, the EC_{50} values were P1/L = 1:22 and P3/L = 1:4 (8), whereas in 1:1 POPE/POPG, they were P1/L = 1:10 and P3/L = 1:3 (25). Hence, the peptides appear to be more membrane-active in

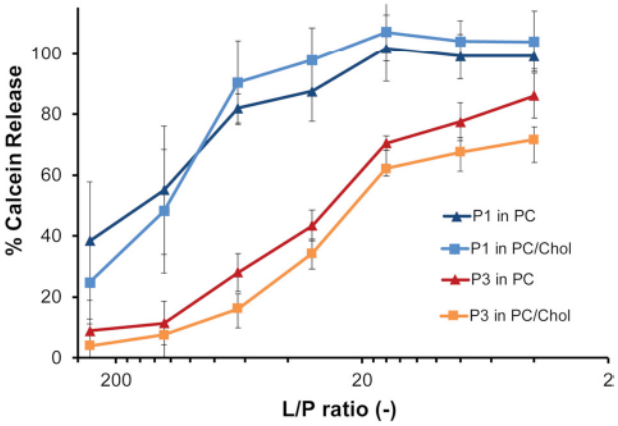

Figure 1. Permeabilization effects of P1 and P3 on POPC and POPC/Chol liposomes. Calcein leakage is plotted for liposomes made of POPC and 4:1 POPC/Chol treated with different amounts of P1 and P3. The EC_{50} values are summarized in Table S1 and compared with previously obtained values in 1:1 POPE/POPG. The % calcein leakage (mean ± S.D.) is displayed as a function of L/P1 and L/P3 for at least six measurements ($n = 6$).

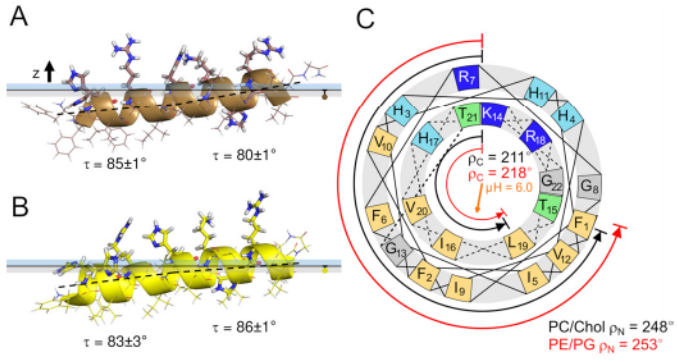

Figure 2. NMR structures of P1 bound to POPC/Chol fluid-oriented multilayers. *A,* structure of P1 bound to 4:1 POPC/Chol fluid bilayers studied at 32 °C (PDB code 6PF0). The NMR samples were prepared at pH 7.4 using a P/L of 1:40. The structure, which represents the lowest-energy member of the ensemble of structural conformers, is displayed for a peptide partitioned in the upper leaflet of the bilayer. Hence, the basic (stick representation) and hydrophobic side chains point upward and downward, respectively. *Gray lines* represent the average position of the C2 atoms of the lipids, based on prior molecular dynamic determinations (42), and *yellow circles* are shown to represent the position of the peptide center of mass. The RMSD between the top 10 structures is 1.14 Å in the α-helical region that experiences no fraying (residues 3–20) (see Table S4). *B,* structure of P1 as solved previously in 1:1 POPE/POPG (PDB code 2MCV) (26). *C,* helical wheel diagram of P1 in 4:1 POPC/Chol. The kink at a central glycine, Gly-13, allows the two halves of the helix to rotate independently around the helical axis, as indicated by different ρ_N and ρ_C values, for the N- and C-terminal regions, respectively (26). *Red arrows* and values represent the rotation angles for P1 in POPE/POPG for comparison, and the *orange arrow* represents the direction of the hydrophobic moment (μH).

bilayers lacking anionic lipids, possibly because the anionic component prevents the peptides from inserting as deeply as in the zwitterionic bilayers, an effect observed for other HDPs (32).

High-resolution structures of P1 and P3 in POPC/Chol

Although the antimicrobial peptide data bank contains more than 3,000 peptides, only 13% have known three-dimensional (3D) structures (33). This is partly explained by the difficulty associated with solving the structures of amphipathic peptides that do not form crystals suitable for structural determination by X-ray diffraction (34, 35). We previously took advantage of oriented sample solid-state NMR to obtain both the structures and orientations of P1 and P3 under native-like conditions, *i.e.* in the presence of hydrated, fluid phospholipid bilayers (26). More precisely, these structures were solved in the presence of 3:1 1,2-dimyristoyl-*sn*-glycero-3-phosphatidylcholine/1,2-dimyristoyl-*sn*-glycero-3-phosphatidylglycerol (DMPC/DMPG) and 1:1 POPE/POPG bilayers as mimics for Gram-positive and -negative bacterial cell membranes (26). Rigorous structural determination of peptide structures in the presence of fluid bilayers requires incorporating the effect of peptide dynamics on the NMR restraints (36–39). As shown for the piscidin structures solved in DMPC/DMPG and POPE/POPG, ^{15}N anisotropic chemical shifts (CSAs) and ^{15}N–^{1}H dipolar couplings (DCs) extracted from two-dimensional spectra of ^{15}N-labeled piscidins provided accurate structural restraints that are highly sensitive to not only secondary structure but also the orientation of the peptides with respect to the bilayer normal. In particular, the ^{15}N–^{1}H DCs exhibit a strong dependence on the tilts of the helical axis (τ) and average azimuthal (ρ) angles adopted by the piscidin peptides bound to bilayers, and thus they can be used to reveal their kinked structures. Furthermore, we demonstrated that all structural restraints are accurate despite peptide dynamics. Here, we solved the structures of P1 and P3 in a binary 4:1 POPC/Chol mixture, as a way to mimic the zwitterionic nature and cholesterol content found in the outer leaflet of mammalian cell membranes (40).

Following the same approach as used previously (26), we obtained ^{15}N–^{1}H DCs and ^{15}N CSAs for P1 and P3 bound to 4:1 POPC/Chol by performing the two-dimensional heteronuclear correlation (HETCOR) experiments (41) on multiple ^{15}N-labeled peptides bound to oriented bilayers. The spectra collected for several multiple-labeled samples of P1 were superimposed to generate Fig. S1.

Fig. 2*A* and Fig. S2*A* show the lowest energy structures that were calculated upon refinement of the NMR restraints collected for P1 and P3 in 4:1 PC/Chol, at P/L = 1:40. Table S4 summarizes the statistics for the calculated structures. The RMSDs for heavy atoms, which are 1.16 and 1.12 Å for P1 and P3, respectively, are based on considering the top 10 structures and focusing on the residues that exhibit α-helicity without fraying, *i.e.* residues 3–20. These RMSD values demonstrate the excellent agreement between the different restraints used for the structural determination.

The structures of P1 and P3 in PC/Chol underscore several important features. First, similarly to the structures determined in PC/PG and PE/PG, those obtained in PC/Chol exhibit highly α-helical and kinked structures, indicating that secondary structure is not significantly affected by membrane composition (26). Kinking in the middle of the peptides is mostly due to the rotation of the helix (characterized by the ρ angle) being different on each side of the conserved glycine at position 13. Such structural imperfection enables the peptides to optimize their hydrophobic moment in the presence of the bilayer (26). As shown in Fig. 2*C* and Fig. S2*C*, the α-helix of P1 is more rotated at its N- than C-terminal end, as reflected by larger ρ_N than ρ_C values, respectively (Table S5). Furthermore, P1 adopts a significantly larger ρ_N value than P3. Hence, ρ is an orienta-

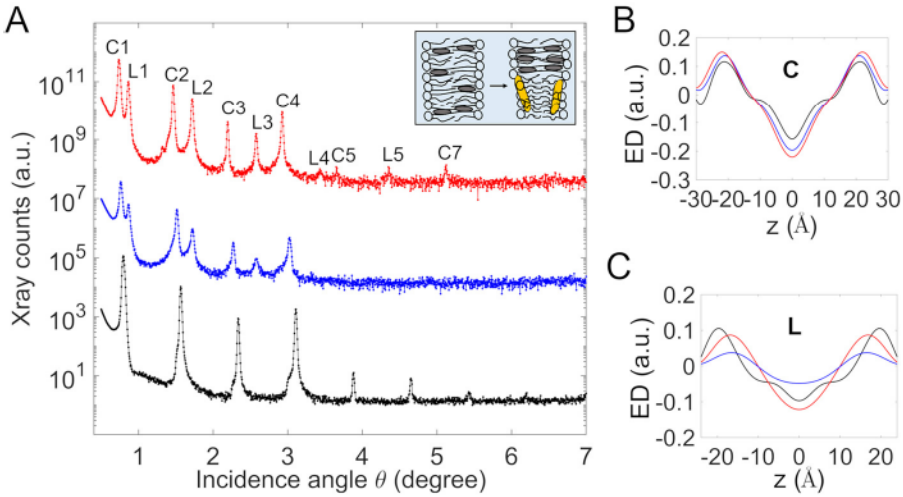

Figure 3. X-ray diffraction data for POPC/Chol in the presence of P1 and P3. *A*, lamellar diffraction from multilayers of a binary mixture 2:1 POPC/Chol without peptides (*black*), with P1 (*blue*), and P3 (*red*). All samples were measured at 98% relative humidity and 25 °C. A Chol-rich phase (*C*) separates from a peptide-rich lipid phase (*L*). Labels show the diffraction order index for the two separate phases. *B*, electron density (*ED*) profiles of the C phase for P1 (*blue*) and P3 (*red*) compared with a profile for a neat 2:1 POPC/Chol bilayer. The corresponding repeat spacing, d (bilayer thickness + water layer) and their standard deviations are as follows: 58.56 (0.12) Å; 60.49 (0.09) Å; and 57.28 (0.03) Å, respectively. *C*, electron density profiles of the L phase for P1 (*blue*) and P3 (*red*) compared with a profile for a neat POPC bilayer. The repeat spacing values are as follows: 51.05 (0.06) Å; 51.52 (0.10) Å; and 53.87 (0.02) Å, for L-P1 and L-P3 and neat POPC, respectively.

tional characteristic that is particularly pertinent to capturing not only the kink at Gly-13 but also the different bilayer arrangements of P1 and P3.

Second, a recurring feature of the bilayer-bound piscidin structures is that, due to subtle changes in the rotation of the helix in the membrane, the side chains are arranged to minimize the footprint of the peptide on the bilayer plane (Table S6 and Fig. S10). This is because most of the bulky hydrophobic residues are grouped together and point straight into the bilayer, although the large polar residues point toward the water phase, leaving the small Gly and Val residues to occupy the sides of the helix (Fig. 2*C*). This distribution gives the peptide the shape of a sharp wedge that may be used to facilitate immersion into the bilayer.

Third, comparing the structures of P1 and P3 in POPC/Chol (4:1) at P/L = 1:40 (Fig. 2*A* and Fig. S2*A*) with those in POPE/POPG (1:1) at P/L = 1:20 (Fig. 2*B* and Fig. S2*B*) reveals that the peptides adopt a more pronounced tilt in the zwitterionic lipids. For P1, it is the C-terminal region that is more tilted in PC/Chol (80 ± 1°) than PE/PG (86 ± 1°), as shown in Fig. 2 *A* and *B*. In contrast, it is the N-terminal end of P3 that is more inclined in PC/Chol (85 ± 1°) than PE/PG (92 ± 1°) (Fig. S2, *A* and *B*). We previously published molecular dynamics data showing that P1 and P3 insert more deeply in the 4:1 POPC/Chol than 1:1 POPE/POPG bilayers (42). Indeed, the depth of insertion for the center of mass of P1 was found to sit 1.0 ± 0.2 and 0.6 ± 0.3 Å below the C2 of the lipid acyl chains in 4:1 POPC/Chol and 1:1 POPE/POPG bilayers, respectively. We used those as guiding values for positioning our structures in Fig. 2. Because the peptides are more lytic in the zwitterionic bilayers, the subtle adjustments in helix rotation and the increased tilting and depth of insertion revealed by our high-resolution structural studies hint that these properties are important for increased membrane activity, as discussed below.

X-ray diffraction studies of POPC/Chol in the presence of P1 and P3

We investigated lamellar samples containing P1 or P3 in the binary mixture of POPC and Chol at various P/L values and POPC/Chol molar ratios by X-ray diffraction. As reported previously (43), PC/Chol binary mixtures at Chol molar fractions of 0.5 or below do not show phase separation. Our data confirm that a mixture of 2:1 POPC/Chol, prepared as oriented multilayers, yields one set of equidistant diffraction peaks corresponding to a homogeneous phase at a single repeat spacing (Fig. 3*A*). Adding P1 or P3 to the POPC/Chol binary mixture causes the appearance of an additional set of Bragg peaks. Partitioning of amphipathic peptides at the bilayer-water interface is expected to thin the bilayer (Fig. S3) due to an area expansion at constant hydrocarbon density, a feature commonly observed in the presence of many membrane-active peptides (44–46). However, Chol clustering with lipids causes lipid-chain ordering and stretching, resulting in a thicker bilayer (47, 48). The mismatch in the thicknesses of the two coexisting phases (domains) in a bilayer together with stacking of like-domains across the multilayers give rise to separate sets of Bragg peaks, explaining the two distinct repeat spacings. The two phases, which differ in bilayer thicknesses by more than 2 Å (Fig. 3*A*, *inset*), can be described as an L_o phase, rich in Chol ("C" phase), and an L_d phase depleted of Chol and enriched with peptide ("L" phase). The C phase displays a slightly thicker bilayer in the presence of peptide, compared with neat (pure) POPC/Chol (Fig. 3*B*). This can be explained by an increased density of Chol in the C region, as Chol is pushed away by the peptide. In contrast, the electron density profiles of the peptide-perturbed L phase (Fig. 3*C*) relative to the pure POPC reveal that the bilayer suffers massive perturbations in the presence of piscidins, with P1 being more disruptive than P3, based on the extent of smearing detected in the profiles. The disorder is so significant that

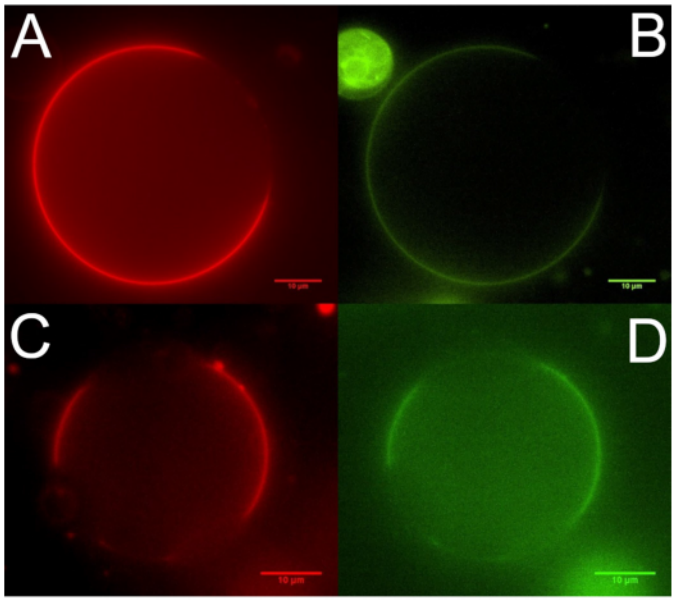

Figure 4. Fluorescence microscopy in GUVs treated with P1 and P3. GUVs are made of raft-forming lipid mixtures with P1 and P3. *A*, P1-TAMRA (*red*). *B*, L_d, phase indicator, Fastdio (*green*). *C*, P3-TAMRA (*red*); and *D*, L_d, phase indicator, Fastdio (*green*). The *dark regions* on the GUV surface correspond to the cholesterol-rich L_o domains. The *scale bars* represent 10 μm.

the segregation of polar–nonpolar regions of the bilayer is almost lost. This is accompanied by a significant bilayer thinning compared with a neat POPC bilayer (Fig. S3).

To further investigate the appearance of two phases in the presence of piscidin, we performed experiments at other P/L and POPC/Chol ratios (Fig. S4, *A* and *B*). We noted that the phase separation persists even at a lower Chol fraction (*e.g.* 4:1 POPC/Chol) if enough peptide is present (P/L >1:25), but it is not observed at lower peptide fractions, including the P/L of 1:40 used for the solid-state NMR structural studies (Fig. S4*B*). This suggests that the separation occurs when the P/L and POPC/Chol reach specific threshold concentrations. Interestingly, at P/L = 1:25, P1 is near the threshold concentration for ~100% dye leakage from POPC and POPC/Chol liposomes (Fig. 1) but only near the leakage midpoint for the POPC/POPG liposomes (8). Thus, phase separation and maximum bilayer disruption appear to be correlated. Overall, these data indicate that both P1 and P3 trigger phase separation in POPC/Chol mixtures with preference for occupying the Chol-depleted L-phase of POPC, thus causing an effective increase in local peptide density. This, in turn, can exacerbate local bilayer deformations and peptide-induced permeabilization as indicated by our neutron diffraction (Fig. 3*C*) and dye-leakage (Fig. 1) data, respectively.

Fluorescence microscopy of P1 and P3 in raft-forming mixtures

To confirm the possibility that piscidin preferentially partitions in the L_d phase, we investigated the partitioning preferences of P1 and P3 in giant unilamellar vesicles (GUVs) prepared from raft-forming lipid/Chol mixtures. The fluorescent lipid FastDio was shown to preferentially partition in the L_d phase (49). As shown in Fig. 4, the location of the TAMRA-labeled peptides (*red*) coincided with the FastDio-labeled lipid (*green*), confirming that both P1 and P3 colocalize with the L_d phase.

X-ray diffraction studies of POPE/POPG mixtures in the presence of P1 and P3

PE and PG lipids are major components of the bacterial membranes, with PE constituting roughly 80% of *E. coli* phospholipids (50). Within the temperature range of 0 to 100 °C, POPE shows two main transitions: a gel–to–fluid (L_β to L_α) transition at 25 °C and a fluid lamellar (L_α) to inverted hexagonal (H_{II}) phase at around 75 °C (Fig. S5*A*), whereas POPG is in a fluid lamellar (L_α) phase. Our diffraction data from lamellar samples made of POPE and POPG show that at temperatures below 25 °C, the gel phase of POPE separates from the fluid phase of POPG (Fig. 5*A*). This behavior changes dramatically in the presence of P1, as the multiple sets of peaks merge into one at temperatures as low as 15 °C (Fig. 5*B*). The gel phase "melts" into a unified fluid phase at temperatures well-below the melting transition for pure POPE. A similar trend is found for P3 (Fig. S6); however, the phase mixing happens at slightly higher temperatures, indicating that P1 is more efficient in altering the phase state behavior of POPE. To uncover the connection between phase behavior and physical location of the peptide in these type of bilayers, we performed differential scanning calorimetry (DSC) measurements coupled with neutron diffraction in PE lipids, as described below.

Differential scanning calorimetry of POPE/POPG and diPoPE in the presence of P1 and P3

Phosphatidylethanolamine (PE) lipids are characterized by cone-shaped molecular geometry, due to the small PE headgroup area compared with the acyl tails. In addition, the PE headgroup can form extensive intermolecular hydrogen bonds with other PE molecules (51). Hence, this lipid possesses a large negative spontaneous curvature (52, 53). These properties make PE lipids prone to packing into a tight gel phase at low temperatures and forming nonlamellar structures at higher temperatures. A gel–to–fluid phase transition is found at T_m = 25 °C for POPE, and at 20 °C for 3:1 POPE/POPG (Fig. S5*A*). Addition of P1 appears to cause "tailing" of this transition toward the low temperature side (Fig. 6*A*). A similar trend is found for P3 (Fig. S5*B*). Other HDPs in similar lipid mixtures were found to produce a splitting into two close transitions, presumably because the cationic peptides segregate with the anionic lipids (54, 55). Although the lipid segregation is not obvious from our DSC scans for P1 (P3), we do notice a broadening of this main transition in the presence of peptides, when compared with the pure POPE/POPG lipid (Fig. 6*A* and Fig. S5*B*). This may explain the accelerated melting of POPE in the presence of piscidin, similar to that caused by increasing the sample temperature.

Because POPE shows an L_α to H_{II} transition at T_H = 75 °C, which is far from physiological temperatures, dipalmitoyl-PE (diPoPE, T_H = 43 °C) can be used for a more amenable detection of this phase transition (56). When we added small amounts of P1 to diPoPE (P/L = 1:350), we detected a strong L_α to H_{II} transition that occurred 5 °C higher compared with pure diPoPE (Fig. 6*B*). The difference suggests that the peptide

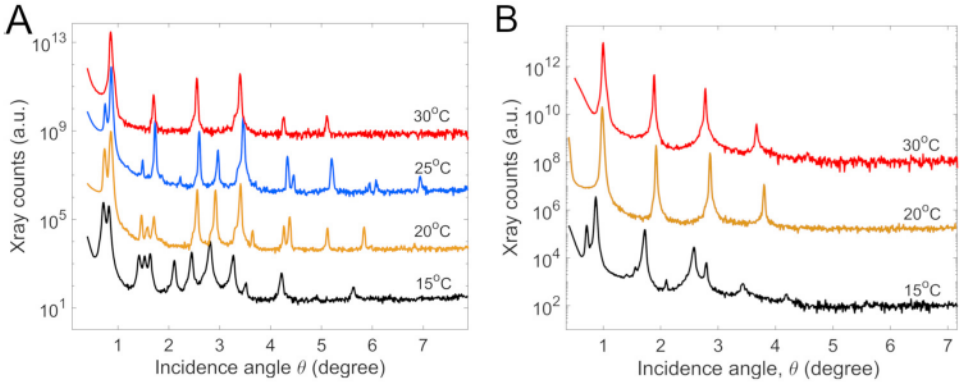

Figure 5. X-ray diffraction data of 3:1 POPE/POPG in the presence of P1. *A,* lamellar diffraction for 3:1 POPE/POPG showing phase separation below 30 °C between POPG in the fluid phase and POPE in the gel phase at temperatures below 30 °C. *B,* same as in *A* for samples with P1 (P/L = 1:25). Samples were measured at 98% relative humidity and were allowed to equilibrate for 1 h after each temperature change. The repeat distances for the homogeneous phase observed at 30 °C are as follows: 52.1 (0.2) Å for 3:1 POPE/POPG and 49.8 (0.1) Å for P1 + 3:1 POPE/POPG.

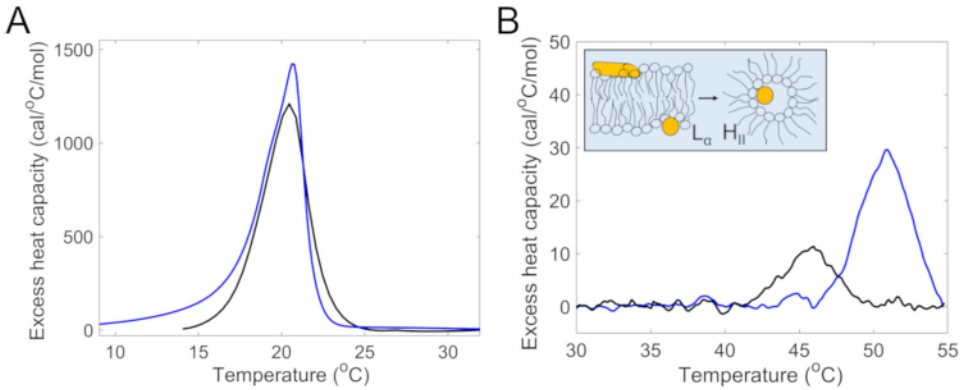

Figure 6. Differential scanning calorimetry in PE lipids. *A,* gel—to—fluid phase transition of 3:1 POPE/POPG without (*black*) and with P1 (*blue*) at P/L = 1:50, upon heating. The peak maxima of the transitions are at 20.5 °C (without P1) and 20.7 °C (with P1). *B,* the lamellar to inverted hexagonal transition is captured for diPoPE (*black*; T = 45.8 °C and ΔH = 47 cal/mol) and P1/diPoPE, at P/L = 1:350 (T = 50.9 °C and ΔH = 121 cal/mol). *Inset:* possible model for the peptide/bilayer assemblies.

imposes positive curvature strain, opposing the intrinsic negative curvature of the lipid, thus delaying the transition to the hexagonal phase. The types of interactions that dominate the association of lipids in the bilayer are as follows: water repulsion from the hydrocarbon region; van der Waals between the hydrocarbon chains; tight solvation of the PE headgroups; and hydrogen bonding between headgroups. Notably, the enthalpy of the L_α to H_{II} transition is larger in the presence of P1 compared with the pure lipid (Fig. 6*B*), indicating that P1 affects the forces acting between the PE lipids. The following question then arises. How would P1 distribute in the bilayer to create such an effect? To answer this question, we employed neutron diffraction and peptide deuterium labeling, as described below.

Neutron diffraction profiles of diPoPE bilayers with deuterated P1

We incorporated a deuterated form of P1 (d_{33}-P1 = $I5_{d10}F6_{d5}$ $L19_{d10}V20_{d8}$) (8) in lamellar samples of diPoPE containing a small amount (5% molar) of POPG or d_{31}-POPG. The incorporation of d_{31}-POPG was needed for a quantitative analysis of the water content by neutron diffraction (Fig. S7) (57). A pair of samples containing P1, in either unlabeled or deuterated (d_{33}-P1) form, were prepared at the same time. The positions and distributions of the deuterated components in the bilayer were calculated using deuterium contrast (58). This included determining the water profile, via $H_2O/^2H_2O$ exchange. Fig. 7 shows the resulting deuterium profiles of P1 label (d_{33}) and water (^2H_2O) relative to the overall profile of the diPoPE bilayer containing P1 in a nondeuterated form. Only one broad deuterium peak, positioned superficially, in the PE headgroup region, can be distinguished. Although two sites on P1 were deuterated, near the N and C termini, the two sites cannot be parsed out in the profile, indicating that the peptide is oriented roughly parallel to the membrane surface. This is to be contrasted with our previous results for P1 in POPC/POPG where a pronounced penetration and tilt in the bilayer could be identified from the distinct positions of the same two deuterated regions (8).

The superficial location of P1 in diPoPE indicates that the interaction is concentrated in the lipid headgroup area. Water colocalizes with the lipid headgroups and the peptide at the water–bilayer interface (Fig. 7). All our studies indicate that P1 has a higher propensity to tilt, insert into, and permeabilize PC-*versus* PE-containing bilayers. Conceivably, contributing factors include the larger area per headgroup for PC *versus* PE (by about 10 Å^2, at full hydration) (59) and the higher headgroup hydration, both of which could facilitate the integration of the amphipathic peptide in the bilayer. Indeed, using deuterium for calibration, we determine here that 8.1 waters associate with

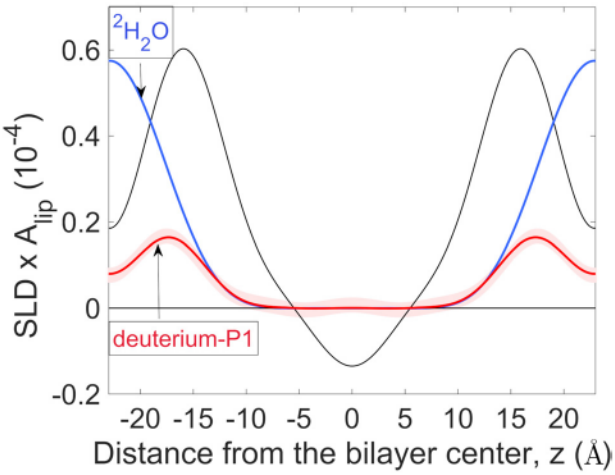

Figure 7. Neutron diffraction profiles for deuterated P1 in diPoPE. Scattering length density profiles determined from neutron lamellar diffraction data (Table S3) for P1 in diPoPE with 5 mol % POPG at P/L = 1:25. Deuterium profiles for deuterated water (*blue*) and deuterated P1 (d_{33}, *red*) were determined by deuterium difference (see under "Experimental procedures"). The ^2H_2O profile includes the exchangeable H on lipid and peptide. The envelope of all deuterium atoms in P1 can be described by a gaussian with the following position and full width at half-maximum: z (d_{33}) = 17.28 (0.18) Å and full width at half-maximum (d_{33}) = 7.88 (0.35) Å. The uncertainty in the parameter values and profile (*pink band*) was determined by a Monte-Carlo sampling procedure (99).

each PE headgroup in diPoPE, compared with 9.4 waters found previously for DOPC (60), both determined at 93% relative humidity. PE has a primary amine in its headgroup, making it capable of forming both intra- and inter-molecular hydrogen bonds. This results in a more densely-packed lipid–water interface compared with a PC membrane, and less room for water and ions to bind. Because P1 resides on the bilayer surface in diPoPE (Fig. 7), it participates in the hydrogen-bonded network with PE headgroups and water. In the H_{II} phase, it was shown that POPE lipid headgroups wrap around water-filled cylindrical channels that are roughly 30 Å in diameter (61). Such channels could accommodate at least one peptide with the helical axis oriented along the cylindrical axis (Fig. 6*B*, *inset*). To allow a change in membrane surface topology, as would be the case in a L_α–to–H_{II} transition, the peptide would need to re-orient its helical axis along the cylindrical axis. Such a peptide re-arrangement could be energetically costly, as suggested by the higher enthalpy for this transition, compared with the pure lipid (Fig. 6*B*). Taken together, our data show that P1 intercalates between the relatively small PE headgroups disrupting the lipid packing (downward shift in T_m) and opposing the natural tendency of the diPoPE to curve (upward shift in T_H).

Patch-clamp experiments using E. coli spheroplasts in the presence of P1 and P3

The above-observed shifts in the lipid phase behavior and domain distributions in membranes upon interaction with P1 create significant changes in the lateral pressure profiles. Such disruptions could affect ion channel behavior in both bacterial and mammalian cell membranes. To explore the possibility of such an effect with P1 and P3, we investigated the behavior of mechanosensitive channels in *E. coli* spheroplasts, treated with both peptides (Fig. 8 and Fig. S8). The integral membrane proteins that are intrinsically designed to sense lateral pressure/tension are called mechanosensitive (MS) channels. MscS and MscL channels, which represent the two most understood tension-gated bacterial osmo-regulatory valves (62), are well-characterized, and thus convenient to detect possible perturbations of the lateral pressure profile in the inner bacterial membrane, where most HDPs deploy their membrane activity.

Fig. 8*A* shows the typical response of a native MS channel population to a linear ramp of pipette pressure (suction). The control curve illustrates two waves of electrical activity: the first wave reflects activation of the low-threshold MscS channels, which saturates, and the second wave represents the population of high-threshold MscL channels. If the shape and curvature of the patch stay constant in the range of activating pressures, the midpoint pressures ($p_{0.5}$) for the MscS and MscL populations directly reflect activating tensions (63). As shown in Fig. 8, the ratio of $p_{0.5}$ (MscS) to $p_{0.5}$ (MscL) is close to 0.6 in the absence of P1. Perfusion of P1 (1.0 μmol/liter) in the chamber bathing the cytoplasmic side of the patch followed by a 15-min equilibration period reproducibly led to a reduction of activation midpoints for both channels. Fig. 8*B* shows values of pressure midpoints normalized to the $p_{0.5}$ (MscL) recorded in response to the first ramp (pull) in the absence of peptide. The second and third ramps were applied to make sure that the patch was stable and that the midpoint did not change substantially with time. After the third ramp, P1, was applied to the bath and after a 15-min equilibration, three more sequential ramps were applied. Some patches mechanically broke under the fifth and the sixth ramp application, and for this reason the number of points on the graph decreased with the number of pulls.

The major information gained from these experiments is that the average mid-point values between the third and fourth pulls decrease in the presence of P1 (Fig. 8*B*). Indeed, the average relative midpoint position shifted from 0.98 ± 0.02 (in the absence of P1) to 0.78 ± 0.09 (in the presence of P1) for MscL and from 0.59 ± 0.01 to 0.50 ± 0.04 for MscS (n = 7). Because the tension midpoint and the in-plane expansion of the channel complex directly reflect the free energy of the opening transition (63), we conclude that for each of these channels the effective transition energy decreased by ~20% in the presence of P1, signifying a substantial change in the way the forces in the lipid bilayer are conveyed to the channels. Fig. S8 illustrates similar experiments performed with P3. Importantly, in all cases we see similar two-wave activation curves and clear unitary MscS currents at the foot of each activation curve signifying that in these curves mechano-activated channel currents are not intermixed with conductances of piscidin-produced pores. The latter appear in *E. coli* patches at substantially higher voltages (Fig. S9). Both peptides showed comparable effects of midpoint reduction at 1.0 μmol/liter. Lower peptide concentrations (0.1–0.5 μmol/liter) produced less reproducible shifts, whereas all tested patches ruptured under mechanical stimulation in the presence of 2 μmol/liter of either peptide, as both exert strong membrane destabilization. These experiments demonstrate the ability of both P1 and P3 to sensitize mechanosensitive channels in bacterial cell membranes, effectively decreasing the energy input of external tension required for the opening tran-

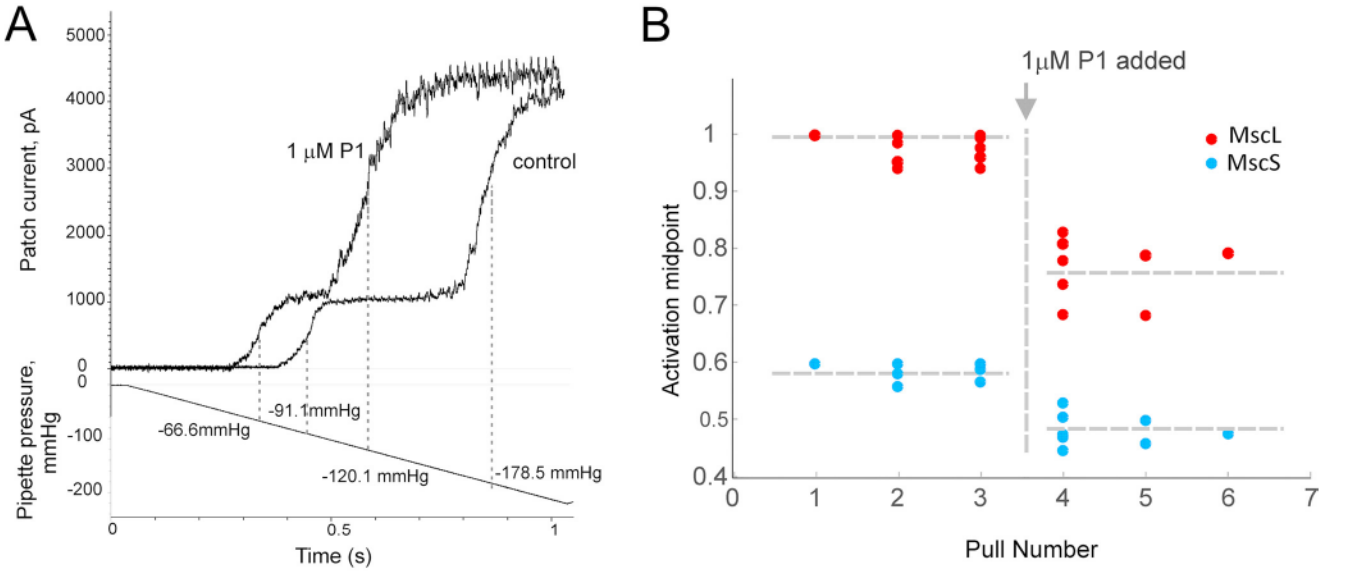

Figure 8. Effect of P1 on the activation of mechanosensitive MscS and MscL channels from the native inner membrane of *E. coli*. Measurements were done in isolated inside-out patches excised from giant spheroplasts at +30-mV pipette voltage (recording buffer: 200 mmol/liter KCl, 90 mmol/liter $MgCl_2$, 10 mmol/liter $CaCl_2$, and 5 mmol/liter HEPES). Each patch was tested with identical linear ramps of pressure before and after introduction of 1.0 μmol/liter of P1 to the cytoplasmic side of the patch. *A,* two-wave current responses reflect activation of MscS population first, followed by a wave of MscL activation. *B,* cumulative data obtained on six independent patches illustrating a substantial decrease of activating (midpoint) pressure for both channels by P1. The midpoint values are normalized to the activation midpoint of MscL in controls. Concentrations of P1 higher than 1 μmol/liter strongly destabilized the patches, making measurements impossible. See text for more details.

sition (63). The observed effects occur at a concentration relevant to the antimicrobial activity of the peptides.

Discussion

Natural membranes are constituted from a variety of lipid species, and their compartmentalization in domains have important biological functions (19, 24). Membrane heterogeneity has received little attention when discussing the mechanisms of action of HDPs. However, it has been observed that anionic lipid clustering caused by cationic HDPs and cell-penetrating peptides can contribute to their mechanism of action (64). P1 differs from other well-studied HDPs in that it exhibits a high adaptability to pH, salinity, and various lipid environments (1, 4–6). This versatility derives partly from P1's capacity to regulate charge across its four histidine residues, thus controlling its hydrophobicity (8) and, as we propose here, its ability to re-organize membrane microenvironments in either bacterial or mammalian cells, resulting in multifaceted modes of membrane disruption.

As part of this study, we solved the high-resolution structures of P1 and P3 bound to fluid bilayers of 4:1 PC/Chol. This information is essential to testing new hypotheses about the modes of action of HDPs and designing novel therapeutics. Although P1 was found to be fully α-helical in SDS micelles (65) and only 45% structured in dodecyl phosphocholine micelles (66), our studies in native-like bilayers confirmed the trend previously obtained in 1:1 PE/PG and 3:1 PC/PG (26); the peptides are highly α-helical and are generally straight, but they are frayed at their extremities and have a kink described by a 25° rotational change between their N- and C-terminal domains. In a recent investigation (8), we showed that the contrasted histidine content of P1 and P3 correlated with their different directionality of membrane insertion, tilts, insertion depths, and membrane permeabilization effects in PC/PG bilayers. Overall, our multiple studies of two homologous peptides in different lipid environments highlight that stronger membranolytic effects are associated with increased tilting and insertion depth and optimization of the helix rotation in the membrane. Importantly, these three properties (tilt, depth of insertion, and helix orientation) vary as a function of the amino acid composition of the peptides and the composition of the membranes.

Although the formation of secondary structure is a major energetic driving force for the binding of amphipathic peptides to membranes (67), flexing at the central Gly-13 further improves amphipathicity. This maximized amphipathicity together with the high ability of P1 for charge regulation associated with its multiple histidines (8) allow the peptide to strongly anchor itself at the hydrophobic–hydrophilic interface in various lipid systems, independently of the presence of anionic lipids. It is, however, interesting to note that P1 permeabilizes membranes with equal efficacy in zwitterionic membranes whether Chol is present or not (Fig. 1), despite the presumed protective role of Chol against lysis. How can this be explained?

Our investigations in lipid membranes of POPC and Chol, major components of the outer leaflet of mammalian cell membranes, clearly show that P1 causes Chol to separate from a POPC/Chol binary mixture by recruiting phospholipids into a fluid phase (Fig. 3) or partitions exclusively into the disordered phase of a raft-forming mixture (Fig. 4). These reorganizations of the membrane can effectively boost the action of P1 because a higher concentration of peptide and larger deformations can occur in the Chol-depleted domains. As a result, the insertion and tilting of the peptide needed to elicit membrane disruption can occur at lower P/L than in homogeneous bilayers. Similar

behaviors were observed for melittin (68) as well as for pardaxin (69) and scorpion HDPs (40) in binary POPC/Chol mixtures. L_d domains in phase-separated (raft-containing) mixtures were shown to be targets for a diverse set of other antimicrobial peptides (70, 71) and also to harbor both fiber and pore formation by the islet amyloid polypeptide (72). Thus, through their ability to induce phase separation even in simple binary POPC/Chol mixtures, piscidins can also create vulnerable sites of accumulation for other toxic peptides. The clear preference of P1/P3 to induce or partition into the L_d phase indicates that the two piscidins prefer the phase where the hydrocarbon chains are more exposed. As we have shown previously, such exposure is reduced in the presence of Chol (47). Notably, the NMR structures reveal that piscidins adopt the shape of a sharp wedge in the bilayer environment, with side chains distributed in a way that minimizes the footprint of the peptide on the bilayer plane (Fig. S10). This allows the peptides to easily anchor themselves between the lipid headgroups at the hydrophilic–hydrophobic interface and more strongly so in the L_d regions.

In the POPE/POPG mixtures used to characterize bacterial membranes, P1 and P3 have the effect of inhibiting the formation of the gel phase of POPE, thus altering the gel/fluid phase transition in a manner comparable with a significant increase in sample temperature. This effect is likely to interfere with the role of PE lipids as key regulators of bacterial membrane fluidity (73), especially in *E. coli* membranes that contain up to 80% PE lipids. Furthermore, our DSC results in diPoPE show that P1 also affects the bilayer morphology by imposing positive curvature strain. A similar effect was observed for the MSI-78 peptide (74) and LL-37 (75). Overall, the observed actions of P1 on PE bilayers, which includes loosening of the lipid packing (Fig. 5) and opposing the PE's intrinsic negative curvature (Fig. 6*B*), are likely to result in significant changes in the lateral pressure patterns in real bacterial membranes.

We show that in *E. coli* spheroplasts the action of P1 on the inner leaflet of the bacterial cytoplasmic membrane leads to the reduction of the midpoint pressures for the activation of both MscS and MscL channels, similar to the action of the ion channel toxin GsMtx4 (76). The lateral pressure profile is difficult to determine experimentally, and extensive molecular dynamics simulation would be needed to describe the local protein–bilayer interactions. Based on the data collected here, we propose two possible explanations for the observed effects. On the one hand, when P1 enters the annular layer of lipids around a mechanosensitive channel, it creates a substantial distortion of this layer, thus re-directing the external tension force that reaches the peripheral segments of the channel through protein–lipid interactions. This effect would likely occur due to the bilayer thinning and changes in the membrane intrinsic curvature causing the channels to perceive compressive forces normal to the plane of the membrane (77), thus leading to their activation at lower mechanical thresholds. Interestingly, addition of conical shape lipids such as lyso-PC to bilayers was found to dramatically lower the activation energies of the eukaryotic mechanosensitive channel (TREK-1 and TRAAK) (78) and drive the prokaryotic MscL into an open conformation (77). By analogy, P1 imposes positive curvature on PE bilayers, resulting in similar effects on the activation of McsL and MscS in the PE-rich *E. coli* membranes. On the other hand, if the peptide becomes a part of the channel–lipid boundary through direct interaction, it may increase the perimeter of this annular zone, thus increasing the total force acting on the channel (force is tension multiplied by perimeter). Effectively, both peptides decrease the energy of the closed–to–open transition by ~25% for MscS (*i.e.* from 24 to 18 kT (79)), and by 33% (from 58 to 38 kT) for MscL (80). The two proposed explanations are similar in the sense that they imply modification of the protein–lipid boundary (direct or indirect), thus re-directing forces acting from the bilayer to the protein. The peptide sub-lethal concentrations tested here lie just below the MIC ranges for *E. coli* (2–10 μmol/liter for P1 and 10–20 μmol/liter for P3). Given the relatively large size of the permeation pores of MscL and MscS, loss of osmolytes through open ion channels can already occur at sub-lethal concentrations and before any peptide forms leakage-competent defects, resulting in bacterial growth inhibition. This may partly explain our previous findings that significant leakage of a small sugar analog molecule occurs through live *E. coli* membranes even at minimal P1 concentrations, well below 1 μmol/liter (25).

Clearly, membrane heterogeneity plays an important role in the overall action of HDPs by creating the ground for preferential localization of HDPs in functionally important membrane regions (*e.g.* regions of high curvature stress and line boundaries) and opportunities for entry and interference with normal cellular processes. Through the examples of the piscidins P1 and P3, and our results in model lipid membranes, we provide evidence that HDPs are able to exploit the heterogeneity of membranes, or otherwise modify the membrane microenvironment to an extent that impairs function of membrane proteins, thus exhibiting multifaceted modes of action against invading cells. Overall, we find that the effects of the piscidins in either cholesterol-rich mammalian or PE-rich bacterial cell membranes feature, as a common ground, the strong promotion of the disordered phase. The resulting changes in lateral pressure profiles (23, 81) can be significant enough to affect the conformations and functional behaviors of transmembrane proteins, including ion channels, and therefore they could offer a possible explanation for the observed anesthetic effect attributed to P1 (11). Furthermore, we show that shifts in the L_o/L_d phase distribution under the action of P1 and P3 can, in turn, influence their permeabilization properties, even at sub-lethal concentrations. This is likely an important but often overlooked mechanism of action for membrane-active HDPs.

Piscidins are especially interesting examples of HDP that show great adaptability, and therefore they may be a good starting model for the design of multipotent peptide treatments. Notably, P1 is very potent against a few lines of human cancer cells (5), many of which are known to contain increased levels of Chol, suggesting a potential use of P1 as a raft-modulating peptide agent for anti-cancer drug development (82–84).

Experimental procedures

Materials

Carboxyamidated P1 (FFHHIFRGIVHVGKTIHRLVTG-NH_2, M_r 2,571) and P3 FIHHIFRGIVHAGRSIGRFLTG-NH_2,

M_r 2,492) were used in all experiments. Unless otherwise indicated, they were obtained from Biomatik USA, LLC (Wilmington, DE) at a purity higher than 98%. Received as hydrochloride salts, the peptides were dialyzed against pure water, and the final concentrations were determined by amino acid analysis. The peptides used in the dye leakage assays, the ^{15}N-labeled peptides used in the NMR experiments, and the ^{2}H-labeled form of P1 (d_{33}-P1 = I5d_{10} F6d_5 L19d_{10} V20d_8) utilized in the neutron diffraction experiments were chemically synthesized at the University of Texas Southwestern Medical Center and purified as reported previously (26). After lyophilization, these peptides were dissolved in dilute HCl and dialyzed to substitute chloride for trifluoroacetate ions, leading to 98% pure peptides. Following reconstitution of the peptides in nanopure water, their molar concentrations were determined by amino acid analysis performed at the Protein Chemistry Center at Texas A&M. Chol (> 99% pure) was purchased from Sigma. Phospholipids were obtained from Avanti Polar Lipids (Alabaster, AL). These include POPC, POPG, d_{31}-POPG, POPE, diPoPE, DOPC, 1,2-dipalmitoyl-*sn*-glycero-3-phosphocholine (DPPC), 1,2-distearoyl-*sn*-glycero-3-phosphocholine (DSPC), and 1,2-dioleoyl-*sn*-glycero-3-phospho-L-serine (DPPS).

Permeabilization assays

Calcein-loaded LUVs were prepared in the presence of P1 and P3, as described previously (25). LUVs contained 4 μmol/liter (total lipid) of 4:1 (mol/mol) POPC/Chol. The assays were performed in 96-well plates by pipetting 180 μl of the LUV suspension and adding 20 μl of the peptide solution. The final lipid concentration in each well was held constant at 10 μmol/liter, although the peptide concentration was varied to cover a range of P/L ratios between 2 and 256. Fluorescence was measured using a Varian (Walnut Creek, CA) Cary Eclipse spectrofluorometer. For the positive control, 20 μl of 1% Triton X-100 was used in place of the peptides.

^{15}N-oriented solid-state NMR

P1 and P3 were reconstituted into oriented 4:1 POPC/Chol bilayers at pH 7.4 (3 mmol/liter phosphate buffer) and a P/L = 1:40 using a procedure reported previously (26, 85). The samples were hydrated 50% by weight. Two-dimensional HETCOR (41) NMR experiments were carried out at the Rensselaer Polytechnic Institute on a Bruker Avance WB600 NMR spectrometer (Larmor frequencies of 600.36 and 60.84 MHz for ^{1}H and ^{15}N, respectively); and at the National High Magnetic Field Laboratory on an ultra-wide bore superconducting a 21.1-T magnet with a Bruker Avance 900 MHz NMR console (Larmor frequencies of 897.11 and 90.92 MHz for ^{1}H and ^{15}N, respectively) and a 14.1-T Bruker Avance WB600 NMR spectrometer (Larmor frequencies of 600.13 and 60.82 MHz for ^{1}H and ^{15}N, respectively). The data were collected at 32.0 ± 0.1 °C using low electrical field double-resonance probes (86) and previously reported parameters (41). The ^{1}H and ^{15}N dimensions were referenced to water at 4.7 ppm and aqueous ^{15}N-labeled ammonium sulfate (5%, pH 3.1) at 0 ppm, respectively.

The HETCOR data were collected for P1 and P3 samples oriented with the bilayer normal is parallel to the static magnetic field, B_0, yielding oriented ^{15}N CSAs and their associated ^{1}H–^{15}N DCs (Fig. S1) as structural and orientational restraints. Multiply- rather than uniformly–^{15}N-labeled samples were used to facilitate the assignments of the signals. Assignments were done in an iterative fashion by fitting the DCs with dipolar waves, as described previously (26). Although the NMR restraints are consistent with two peptide orientations related by a 180° rotation about the z axis (B_0 static field), only one orientation allows the peptide to orient its nonpolar residues toward the bilayer interior.

Structure determination

Refined NMR structures were calculated using XPLOR–NIH (87, 88) run within the NMRBox virtual environment (89). Simulated annealing was performed by reducing the temperature from the initial value of 2,000 to 50 K in steps of 12.5 K. Ideal ϕ/ψ angle restraints (−61°/−45°) with ±5° variations were used for residues 1–21 with k_{ta} ramped from 100 to 300 kcal·mol^{-1}·rad^{-2}. k_{rdc} was gradually increased from 0.5 to 1 kcal·mol^{-1}·s^2, and k_{CSA} was set constant at 0.1 kcal·mol^{-1}·s^2 in order to be consistent with the experimental error. These force constants, which correspond to a final CSA_{scale}/DC_{scale} of 0.1, were chosen to obtain the optimal balance between the effects of the DC and CSA restraints in the structure calculations (88, 90). The NMR restraints used in XPLOR–NIH came from the HETCOR spectra collected on each peptide. To match the experimental conditions, the orientation tensor axial component D_a was set to an initial value of 10.4 kHz and refined to ~10.0 kHz for P1 and 9.9 kHz for P3. Rhombicity was fixed at zero for all calculations. The calculation also included the XPLOR–NIH potential for knowledge-based torsion angles with ramped force constants of 0.002 to 1 kcal·mol^{-1}·rad^{-2}. The calculation also used the implicit solvent potential eefxPot (91, 92), with terms for Lennard-Jones van der Waals energy (E_{vdW}), electrostatic energy (E_{Elec}), and solvation-free energy (E_{Slv}). The eefxPot potential was incorporated to model the membrane–water interface, with the membrane thickness (T) set to 25 Å, the dielectric screening scaling factor (a) set to 0.85, and the profile exponent (n) set to 10. The initial position of the peptide was set at 15 Å from the center of the bilayer potential. The eefxPot scaling factor was set to an initial value of 0.1 at high temperature and ramped up to 1 during simulated annealing. Routine terms ANGL, BOND, and IMPR were also added to the calculation. A total of 100 structures were generated, and the 10 lowest-energy structures were accepted for analysis and representation. We note that these parameters were previously used to successfully refine the structure of P3 in PC/PG (92). The atomic coordinates for the 10 lowest-energy structures of the two systems have been deposited in the Protein Data Bank with ID numbers 6PF0 (P1) and 6PEZ (P3). Structure figures were generated using PyMOL (The PyMOL Molecular Graphics System, Version 1.3, Schrödinger, LLC). Helical wheel diagrams were generated using the tool available online at http://helix.perrinresearch.com/wheels/.[5]

[5] Please note that the JBC is not responsible for the long-term archiving and maintenance of this site or any other third party hosted site.

Neutron and X-ray diffraction

Lipids (2 mg) were dissolved in chloroform and mixed with peptides in trifluoroethanol (TFE) (Acros Organics) to the desired P/L. After evaporating the organic solvents under a flow of nitrogen, the samples were dried under vacuum for 1 h, thoroughly hydrated with nanopure water in a shaker at 35 °C for 1 h, and then spread on thin glass coverslips. The bulk water was allowed to evaporate slowly overnight at room temperature. Before the diffraction experiments, the samples were annealed at 98% relative humidity and 30 °C for at least 12 h. For additional controls, POPC/Chol mixtures without peptide were prepared in H_2O as above, and water-solubilized P1 (P3) was subsequently added to the preformed lipid vesicles at the desired P/L. Samples containing diPoPE lipid were prepared directly from organic solvent because of their poor solubility in water, particularly at high concentrations. Deuterium-containing and natural abundance samples of P1 were prepared in parallel. Lamellar neutron diffraction sets, probing the direction orthogonal to the bilayer plane, were acquired with the instrument MAGIk at the National Institute of Standards and Technology Center for Neutron Research, Gaithersburg, MD. The data were processed and analyzed as described before (46, 47). Tables with structure factors can be found in (Tables S2 and S3). Repeat spacings and their uncertainties were determined by a linear fit of the Bragg peak position *versus* diffraction order.

X-ray diffraction measurements were performed on a 3-kW Rigaku Smartlab diffractometer located at the Institute for Bioscience and Biotechnology Research (IBBR), Rockville, MD. Phases of the structure factors were determined by the swelling method (93). Structure factors were calculated from the integrated Bragg intensities after subtracting background and applying Lorentz, polarization, beam footprint, and absorption corrections. Electron density profiles were computed on an arbitrary scale, using direct Fourier reconstruction (94).

Fluorescence microscopy

GUVs were prepared at 84 mM in buffer (20 mmol/liter Tris, 50 mmol/liter NaCl, 127 mmol/liter sucrose, pH 7.4) using a previously described protocol (95, 96). To yield liquid ordered and disordered domains, two lipid compositions were used: 17.8:12.2:30.0:15.0:25.00 DSPC/DPPS/DOPC/1,2-dioleoyl-*sn*-glycero-3-phospho-L-serine/Chol and 17.8:45.0:12.2:25.0 DSC/DOPC/DPPS/Chol (96). The fluorescent lipid FastDio, which preferentially partitions in the L_d phase, was added at 0.1 mol % (49). Following the formation of GUVs, 370 nmol/liter TAMRA-P1 or 540 nmol/liter TAMRA-P3 was added. Imaging was performed at 23 °C on a Nikon Eclipse Ti microscope (Nikon Instruments, Melville, NY). Filters were used to avoid artifacts. Data were processed in ImageJ.

Differential scanning calorimetry

Samples were prepared as above by co-dissolving the peptide and lipid in TFE/chloroform. The organic solvent was removed under a stream of nitrogen gas, and placed under vacuum for 2 h. The dry lipid/peptide mixtures were resuspended in ultrapure water and allowed to hydrate overnight with continuous shaking. Alternatively, PIPES buffer was used (10 mmol/liter PIPES, 50 mmol/liter NaCl, phosphate, 0.5 mmol/liter EDTA, pH 7.4) for preparations of diPoPE samples, resulting in noisier data (Fig. S5*D*). The samples were measured at a lipid concentration of 2.5 mg/ml. DSC measurements were made on VP-DSC microcalorimeter (MicroCal Inc., Northampton, MA). Six scans were made at a scan rate of 30 °C/h. There was a 15-min equilibrating period prior to starting the experiment and a delay of 5 min between sequential scans to allow for thermal equilibration. DSC curves were analyzed by Origin, version 7.0 (OriginLab Corp.).

Patch-clamp measurements on giant E. coli spheroplasts

WT *E. coli* strain Frag-1, which natively expresses the mechanosensitive channels MscS and MscL as two dominant and readily observable species, was used in the patch-clamp experiments (97, 98). Giant spheroplasts were prepared from Frag-1 cells using the standard steps of filamentous growth in the presence of cephalexin followed by cell wall digestion with lysozyme in the presence of EDTA, as described previously (79). Patch pipettes were pulled from borosilicate glass capillaries (Drummond Scientific no. 2-000-100) to the inner diameter of ~1.5 μm and used without fire polishing or coating. All measurements were done in inside-out excised patches. Stimulating pressure protocols (linear suction ramps) were delivered from a pressure-clamp apparatus (ALA Instruments, Farmingdale, NY) and programmed in the PClamp-10 software (Molecular Devices, San Jose, CA). The standard spheroplast recording buffer contained (in mmol/liter) 200 KCl, 10 $CaCl_2$, 90 $MgCl_2$, and 5 HEPES, pH 7.2. Currents were measured using Axopatch 200B amplifier (Molecular Devices) at 30-mV pipette voltage in most experiments. The current and pressure traces were recorded simultaneously, and the analysis of activation midpoint pressures was done using PClamp-10 software. To ensure stability and constant midpoints of the excised patches, three linear ramp pulls were done before the addition of any peptide. For surviving patches, P1/P3 was added between the third and fourth pull and allowed to equilibrate for 15 min before pulls were resumed for a total of six measurements.

Author contributions—F. C., A. G., J. M., R. A., L. L., T. K., L. S. C., Y. W., R. F., J. H., J. B., S. S., M. L. C., and M. M. investigation; F. C., A. G., S. S., M. L. C., and M. M. methodology; F. C., A. G., S. S., M. L. C., and M. M. writing-review and editing; S. S., M. L. C., and M. M. supervision; M. L. C. formal analysis; M. L. C. and M. M. funding acquisition; M. L. C. and M. M. project administration; M. L. C. and M. M. conceptualization; M. M. writing-original draft.

Acknowledgments—We are grateful for the NMR time awarded by the National High Magnetic Field Laboratory supported by National Science Foundation Cooperative Agreement DMR-1644779, the State of Florida, and the United States Department of Energy. We thank Prof. Gerald W. Feigenson (Cornell University) for help with fluorescence measurements in GUVs. This study utilized neutron diffraction facilities at the United States National Institute of Standards and Technology, Gaithersburg, MD. This study made use of NMRbox: National Center for Biomolecular NMR Data Processing and Analysis, a Biomedical Technology Research Resource, which is supported by National Institutes of Health NIGMS Grant P41GM111135. The identification of any commercial product or trade name does not imply endorsement or recommendation by the National Institute of Standards and Technology.

References

1. Lauth, X., Shike, H., Burns, J. C., Westerman, M. E., Ostland, V. E., Carlberg, J. M., Van Olst, J. C., Nizet, V., Taylor, S. W., Shimizu, C., and Bulet, P. (2002) Discovery and characterization of two isoforms of moronecidin, a novel antimicrobial peptide from hybrid striped bass. *J. Biol. Chem.* **277,** 5030–5039 CrossRef Medline
2. Silphaduang, U., Colorni, A., and Noga, E. J. (2006) Evidence for widespread distribution of piscidin antimicrobial peptides in teleost fish. *Dis. Aquat. Organ.* **72,** 241–252 CrossRef Medline
3. Silphaduang, U., and Noga, E. J. (2001) Peptide antibiotics in mast cells of fish. *Nature* **414,** 268–269 CrossRef Medline
4. Wang, G. (2013) Database-guided discovery of potent peptides to combat HIV-1 or superbugs. *Pharmaceuticals* **6,** 728–758 CrossRef Medline
5. Lin, H. J., Huang, T. C., Muthusamy, S., Lee, J. F., Duann, Y. F., and Lin, C. H. (2012) Piscidin-1, an antimicrobial peptide from fish (hybrid striped bass *Morone saxatilis* x *M. chrysops*), induces apoptotic and necrotic Activity in HT1080 cells. *Zoolog. Sci.* **29,** 327–332 CrossRef Medline
6. Mao, Y., Niu, S., Xu, X., Wang, J., Su, Y., Wu, Y., and Zhong, S. (2013) The effect of adding histidine on biological activity and stability of Pc-pis from *Pseudosciaena crocea*. *PLoS ONE* **8,** e83268 CrossRef Medline
7. Mulero, I., Noga, E. J., Meseguer, J., García-Ayala, A., and Mulero, V. (2008) The antimicrobial peptides piscidins are stored in the granules of professional phagocytic granulocytes of fish and are delivered to the bacteria-containing phagosome upon phagocytosis. *Dev. Comp. Immunol.* **32,** 1531–1538 CrossRef Medline
8. Mihailescu, M., Sorci, M., Seckute, J., Silin, V. I., Hammer, J., Perrin, B. S., Jr., Hernandez, J. I., Smajic, N., Shrestha, A., Bogardus, K. A., Greenwood, A. I., Fu, R., Blazyk, J., Pastor, R. W., Nicholson, L. K., Belfort, G., and Cotten, M. L. (2019) Structure and function in antimicrobial piscidins: histidine position, directionality of membrane insertion, and pH-dependent permeabilization. *J. Am. Chem. Soc.* **141,** 9837–9853 CrossRef Medline
9. Wade, D., Boman, A., Wåhlin, B., Drain, C. M., Andreu, D., Boman, H. G., and Merrifield, R. B. (1990) All-D amino acid-containing channel-forming antibiotic peptides. *Proc. Natl. Acad. Sci. U.S.A.* **87,** 4761–4765 CrossRef Medline
10. Suchyna, T. M., Tape, S. E., Koeppe, R. E., 2nd, Andersen, O. S., Sachs, F., and Gottlieb, P. A. (2004) Bilayer-dependent inhibition of mechanosensitive channels by neuroactive peptide enantiomers. *Nature* **430,** 235–240 CrossRef Medline
11. Chen, W. F., Huang, S. Y., Liao, C. Y., Sung, C. S., Chen, J. Y., and Wen, Z. H. (2015) The use of the antimicrobial peptide piscidin (PCD)-1 as a novel anti-nociceptive agent. *Biomaterials* **53,** 1–11 CrossRef Medline
12. Kim, S. Y., Zhang, F., Gong, W., Chen, K., Xia, K., Liu, F., Gross, R., Wang, J. M., Linhardt, R. J., and Cotten, M. L. (2018) Copper regulates the interactions of antimicrobial piscidin peptides from fish mast cells with formyl peptide receptors and heparin. *J. Biol. Chem.* **293,** 15381–15396 CrossRef Medline
13. Glukhov, E., Stark, M., Burrows, L. L., and Deber, C. M. (2005) Basis for selectivity of cationic antimicrobial peptides for bacterial *versus* mammalian membranes. *J. Biol. Chem.* **280,** 33960–33967 CrossRef Medline
14. van Meer, G., Voelker, D. R., and Feigenson, G. W. (2008) Membrane lipids: where they are and how they behave. *Nat. Rev. Mol. Cell. Biol.* **9,** 112–124 CrossRef Medline
15. Epand, R. M., and Epand, R. F. (2011) Bacterial membrane lipids in the action of antimicrobial agents. *J. Peptide Sci.* **17,** 298–305 CrossRef Medline
16. Matsuzaki, K., Sugishita, K., Fujii, N., and Miyajima, K. (1995) Molecular basis for membrane selectivity of an antimicrobial peptide, magainin 2. *Biochemistry* **34,** 3423–3429 CrossRef Medline
17. Benachir, T., Monette, M., Grenier, J., and Lafleur, M. (1997) Melittin-induced leakage from phosphatidylcholine vesicles is modulated by cholesterol: a property used for membrane targeting. *Eur. Biophys. J.* **25,** 201–210 CrossRef
18. Katsu, T., Kuroko, M., Morikawa, T., Sanchika, K., Yamanaka, H., Shinoda, S., and Fujita, Y. (1990) Interaction of wasp venom mastoparan with biomembranes. *Biochim. Biophys. Acta* **1027,** 185–190 CrossRef Medline
19. Simons, K., and Ikonen, E. (1997) Functional rafts in cell membranes. *Nature* **387,** 569–572 CrossRef Medline
20. Petersen, E. N., Chung, H. W., Nayebosadri, A., and Hansen, S. B. (2016) Kinetic disruption of lipid rafts is a mechanosensor for phospholipase D. *Nat. Commun.* **7,** 13873 CrossRef Medline
21. Pavel, M. A., Petersen, E. N., Lerner, R. A., and Hansen, S. B. (2018) Studies on the mechanism of general anesthesia. *bioRxiv* CrossRef
22. Weinrich, M., and Worcester, D. L. (2013) Xenon and other volatile anesthetics change domain structure in model lipid raft membranes. *J. Phys. Chem. B.* **117,** 16141–16147 CrossRef Medline
23. Cantor, R. S. (1997) Lateral pressures in cell membranes: A mechanism for modulation of protein function. *J. Phys. Chem. B.* **101,** 1723–1725 CrossRef
24. Strahl, H., and Errington, J. (2017) Bacterial membranes: structure, domains, and function. *Annu. Rev. Microbiol.* **71,** 519–538 CrossRef Medline
25. Hayden, R. M., Goldberg, G. K., Ferguson, B. M., Schoeneck, M. W., Libardo, M. D., Mayeux, S. E., Shrestha, A., Bogardus, K. A., Hammer, J., Pryshchep, S., Lehman, H. K., McCormick, M. L., Blazyk, J., Angeles-Boza, A. M., Fu, R., and Cotten, M. L. (2015) Complementary effects of host-defense peptides piscidin 1 and piscidin 3 on DNA and lipid membranes: biophysical insights into contrasting biological activities. *J. Phys. Chem. B.* **119,** 15235–15246 CrossRef Medline
26. Perrin, B. S., Jr., Tian, Y., Fu, R., Grant, C. V., Chekmenev, E. Y., Wieczorek, W. E., Dao, A. E., Hayden, R. M., Burzynski, C. M., Venable, R. M., Sharma, M., Opella, S. J., Pastor, R. W., and Cotten, M. L. (2014) High-resolution structures and orientations of antimicrobial peptides piscidin 1 and piscidin 3 in fluid bilayers reveal tilting, kinking, and bilayer immersion. *J. Am. Chem. Soc.* **136,** 3491–3504 CrossRef Medline
27. Brogden, K. A. (2005) Antimicrobial peptides: pore formers or metabolic inhibitors in bacteria? *Nat. Rev. Microbiol.* **3,** 238–250 CrossRef Medline
28. Shai, Y. (2002) Mode of action of membrane active antimicrobial peptides. *Biopolymers* **66,** 236–248 CrossRef Medline
29. Guha, S., Ghimire, J., Wu, E., and Wimley, W. C. (2019) Mechanistic landscape of membrane-permeabilizing peptides. *Chem. Rev.* **119,** 6040–6085 CrossRef Medline
30. Faust, J. E., Yang, P.-Y., and Huang, H. W. (2017) Action of antimicrobial peptides on bacterial and lipid membranes: a direct comparison. *Biophys. J.* **112,** 1663–1672 CrossRef Medline
31. Sochacki, K. A., Barns, K. J., Bucki, R., and Weisshaar, J. C. (2011) Real-time attack on single *Escherichia coli* cells by the human antimicrobial peptide LL-37. *Proc. Natl. Acad. Sci. U.S.A.* **108,** E77–E81 CrossRef Medline
32. Strömstedt, A. A., Wessman, P., Ringstad, L., Edwards, K., and Malmsten, M. (2007) Effect of lipid headgroup composition on the interaction between melittin and lipid bilayers. *J. Colloid Interface Sci.* **311,** 59–69 CrossRef Medline
33. Wang, G., Li, X., and Wang, Z. (2009) APD2: the updated antimicrobial peptide database and its application in peptide design. *Nucleic Acids Res.* **37,** D933–D937 CrossRef Medline
34. Hwang, P. M., and Vogel, H. J. (1998) Structure–function relationships of antimicrobial peptides. *Biochem. Cell Biol.* **76,** 235–246 CrossRef Medline
35. Ramamoorthy, A. (2010) NMR structural insights on the function of antimicrobial peptides. *Abstracts–Papers of the American Chemical Society* **240**
36. Fu, R., and Cross, T. A. (1999) Solid-state NMR investigation of protein and polypeptide structure. *Annu. Rev. Biophys. Biomol. Struct.* **28,** 235–268 CrossRef Medline
37. Opella, S. J., and Marassi, F. M. (2004) Structure determination of membrane proteins by NMR spectroscopy. *Chem. Rev.* **104,** 3587–3606 CrossRef Medline
38. Bechinger, B., and Salnikov, E. S. (2012) The membrane interactions of antimicrobial peptides revealed by solid-state NMR spectroscopy. *Chem. Phys. Lipids* **165,** 282–301 CrossRef Medline
39. Hong, M., and Su, Y. (2011) Structure and dynamics of cationic membrane peptides and proteins: insights from solid-state NMR. *Protein Sci.* **20,** 641–655 CrossRef Medline

40. Luna-Ramirez, K., Sani, M. A., Silva-Sanchez, J., Jiménez-Vargas, J. M., Reyna-Flores, F., Winkel, K. D., Wright, C. E., Possani, L. D., and Separovic, F. (2014) Membrane interactions and biological activity of antimicrobial peptides from Australian scorpion. *Biochim. Biophys. Acta* **1838,** 2140–2148 CrossRef Medline
41. Fu, R., Gordon, E. D., Hibbard, D. J., and Cotten, M. (2009) High resolution heteronuclear correlation NMR spectroscopy of an antimicrobial peptide in aligned lipid bilayers: peptide–water interactions at the water–bilayer interface. *J. Am. Chem. Soc.* **131,** 10830–10831 CrossRef Medline
42. Perrin, B. S., Jr., Sodt, A. J., Cotten, M. L., and Pastor, R. W. (2015) The curvature induction of surface-bound antimicrobial peptides piscidin 1 and piscidin 3 varies with lipid chain length. *J. Membr. Biol.* **248,** 455–467 CrossRef Medline
43. Bach, D., and Wachtel, E. (2003) Phospholipid/cholesterol model membranes: formation of cholesterol crystallites. *Biochim. Biophys. Acta* **1610,** 187–197 CrossRef Medline
44. Ludtke, S., He, K., and Huang, H. (1995) Membrane thinning caused by magainin 2. *Biochemistry* **34,** 16764–16769 CrossRef Medline
45. Hristova, K., Dempsey, C. E., and White, S. H. (2001) Structure, location, and lipid perturbations of melittin at the membrane interface. *Biophys. J.* **80,** 801–811 CrossRef Medline
46. Mihailescu, M., Krepkiy, D., Milescu, M., Gawrisch, K., Swartz, K. J., and White, S. (2014) Structural interactions of a voltage sensor toxin with lipid membranes. *Proc. Natl. Acad. Sci. U.S.A.* **111,** E5463–E70 CrossRef Medline
47. Mihailescu, M., Vaswani, R. G., Jardón-Valadez, E., Castro-Román, F., Freites, J. A., Worcester, D. L., Chamberlin, A. R., Tobias, D. J., and White, S. H. (2011) Acyl-chain methyl distributions of liquid-ordered and -disordered membranes. *Biophys. J.* **100,** 1455–1462 CrossRef Medline
48. Worcester, D. L., and Franks, N. P. (1976) Structural-analysis of hydrated egg lecithin and cholesterol bilayers. 2. Neutron-diffraction. *J. Mol. Biol.* **100,** 359–378 CrossRef Medline
49. Wen, Y., Dick, R. A., Feigenson, G. W., and Vogt, V. M. (2016) Effects of membrane charge and order on membrane binding of the retroviral structural protein Gag. *J. Virol.* **90,** 9518–9532 CrossRef Medline
50. Sohlenkamp, C., and Geiger, O. (2016) Bacterial membrane lipids: diversity in structures and pathways. *FEMS Microbiol. Rev.* **40,** 133–159 CrossRef Medline
51. Pink, D. A., McNeil, S., Quinn, B., and Zuckermann, M. J. (1998) A model of hydrogen bond formation in phosphatidylethanolamine bilayers. *Biochim. Biophys. Acta* **1368,** 289–305 CrossRef Medline
52. Gruner, S. M. (1989) Stability of lyotropic phases with curved interfaces. *J. Phys. Chem.* **93,** 7562–7570 CrossRef
53. Israelachvili, J. N., Marcelja, S., and Horn, R. G. (1980) Physical principles of membrane organization. *Q. Rev. Biophys.* **13,** 121–200 CrossRef Medline
54. Lohner, K., and Prenner, E. J. (1999) DIfferential scanning calorimetry and x-ray diffraction studies of the specificity of the interaction of antimicrobial peptides with membrane-mimetic systems. *Biochim. Biophys. Acta* **1462,** 141–156 CrossRef Medline
55. Epand, R. F., Maloy, W. L., Ramamoorthy, A., and Epand, R. M. (2010) Probing the "charge cluster mechanism" in amphipathic helical cationic antimicrobial peptides. *Biochemistry* **49,** 4076–4084 CrossRef Medline
56. Matsuzaki, K., Sugishita, K., Ishibe, N., Ueha, M., Nakata, S., Miyajima, K., and Epand, R. M. (1998) Relationship of membrane curvature to the formation of pores by magainin 2. *Biochemistry* **37,** 11856–11863 CrossRef Medline
57. Blasic, J. R., Worcester, D. L., Gawrisch, K., Gurnev, P., and Mihailescu, M. (2015) Pore hydration states of KcsA potassium channels in membranes. *J. Biol. Chem.* **290,** 26765–26775 CrossRef Medline
58. Franks, N. P., Arunachalam, T., and Caspi, E. (1978) A direct method for determination of membrane electron density profiles on an absolute scale. *Nature* **276,** 530–532 CrossRef Medline
59. Kučerka, N., van Oosten, B., Pan, J., Heberle, F. A., Harroun, T. A., and Katsaras, J. (2015) Molecular structures of fluid phosphatidylethanolamine bilayers obtained from simulation–to–experiment comparisons and experimental scattering density profiles. *J. Phys. Chem. B.* **119,** 1947–1956 CrossRef Medline
60. Hristova, K., and White, S. H. (1998) Determination of the hydrocarbon core structure of fluid dioleoylphosphocholine (DOPC) bilayers by x-ray diffraction using specific bromination of the double-bonds: effect of hydration. *Biophys. J.* **74,** 2419–2433 CrossRef Medline
61. Rappolt, M., Hickel, A., Bringezu, F., and Lohner, K. (2003) Mechanism of the lamellar/inverse hexagonal phase transition examined by high resolution x-ray diffraction. *Biophys. J.* **84,** 3111–3122 CrossRef Medline
62. Kung, C., Martinac, B., and Sukharev, S. (2010) Mechanosensitive channels in microbes. *Annu. Rev. Microbiol.* **64,** 313–329 CrossRef Medline
63. Sukharev, S. I., Sigurdson, W. J., Kung, C., and Sachs, F. (1999) Energetic and spatial parameters for gating of the bacterial large conductance mechanosensitive channel, MscL. *J. Gen. Physiol.* **113,** 525–540 CrossRef Medline
64. Wadhwani, P., Epand, R. F., Heidenreich, N., Bürck, J., Ulrich, A. S., and Epand, R. M. (2012) Membrane-active peptides and the clustering of anionic lipids. *Biophys. J.* **103,** 265–274 CrossRef Medline
65. Lee, S. A., Kim, Y. K., Lim, S. S., Zhu, W. L., Ko, H., Shin, S. Y., Hahm, K. S., and Kim, Y. (2007) Solution structure and cell selectivity of piscidin 1 and its analogues. *Biochemistry* **46,** 3653–3663 CrossRef Medline
66. Campagna, S., Saint, N., Molle, G., and Aumelas, A. (2007) Structure and mechanism of action of the antimicrobial peptide piscidin. *Biochemistry* **46,** 1771–1778 CrossRef Medline
67. Wimley, W. C., and White, S. H. (1996) Experimentally determined hydrophobicity scale for proteins at membrane interfaces. *Nat. Struct. Biol.* **3,** 842–848 CrossRef Medline
68. Wessman, P., Strömstedt, A. A., Malmsten, M., and Edwards, K. (2008) Melittin-lipid bilayer interactions and the role of cholesterol. *Biophys. J.* **95,** 4324–4336 CrossRef Medline
69. Epand, R. F., Ramamoorthy, A., and Epand, R. M. (2006) Membrane lipid composition and the interaction of pardaxin: the role of cholesterol. *Protein Pept. Lett.* **13,** 1–5 Medline
70. Pokorny, A., and Almeida, P. F. (2005) Permeabilization of raft-containing lipid vesicles by δ-lysin: a mechanism for cell sensitivity to cytotoxic peptides. *Biochemistry* **44,** 9538–9544 CrossRef Medline
71. McHenry, A. J., Sciacca, M. F., Brender, J. R., and Ramamoorthy, A. (2012) Does cholesterol suppress the antimicrobial peptide induced disruption of lipid raft containing membranes? *Biochim. Biophys. Acta* **1818,** 3019–3024 CrossRef Medline
72. Sciacca, M. F., Lolicato, F., Di Mauro, G., Milardi, D., D'Urso, L., Satriano, C., Ramamoorthy, A., and La Rosa, C. (2016) The role of cholesterol in driving IAPP-membrane interactions. *Biophys. J.* **111,** 140–151 CrossRef Medline
73. Dawaliby, R., Trubbia, C., Delporte, C., Noyon, C., Ruysschaert, J. M., Van Antwerpen, P., and Govaerts, C. (2016) Phosphatidylethanolamine is a key regulator of membrane fluidity in eukaryotic cells. *J. Biol. Chem.* **291,** 3658–3667 CrossRef Medline
74. Hallock, K. J., Lee, D. K., and Ramamoorthy, A. (2003) MSI-78, an analogue of the magainin antimicrobial peptides, disrupts lipid bilayer structure via positive curvature strain. *Biophys. J.* **84,** 3052–3060 CrossRef Medline
75. Henzler Wildman, K. A., Lee, D. K., and Ramamoorthy, A. (2003) Mechanism of lipid bilayer disruption by the human antimicrobial peptide, LL-37. *Biochemistry* **42,** 6545–6558 CrossRef Medline
76. Kamaraju, K., Gottlieb, P. A., Sachs, F., and Sukharev, S. (2010) Effects of GsMTx4 on bacterial mechanosensitive channels in inside-out patches from giant spheroplasts. *Biophys. J.* **99,** 2870–2878 CrossRef Medline
77. Perozo, E., Kloda, A., Cortes, D. M., and Martinac, B. (2002) Physical principles underlying the transduction of bilayer deformation forces during mechanosensitive channel gating. *Nat. Struct. Biol.* **9,** 696–703 CrossRef Medline
78. Maingret, F., Patel, A. J., Lesage, F., Lazdunski, M., and Honoré, E. (2000) Lysophospholipids open the two-pore domain mechano-gated K^+ channels TREK-1 and TRAAK. *J. Biol. Chem.* **275,** 10128–10133 CrossRef Medline
79. Akitake, B., Anishkin, A., and Sukharev, S. (2005) The "dashpot" mechanism of stretch-dependent gating in MscS. *J. Gen. Physiol.* **125,** 143–154 CrossRef Medline

80. Chiang, C. S., Anishkin, A., and Sukharev, S. (2004) Gating of the large mechanosensitive channel *in situ*: estimation of the spatial scale of the transition from channel population responses. *Biophys. J.* **86,** 2846–2861 CrossRef Medline
81. Gruner, S. M., and Shyamsunder, E. (1991) Is the mechanism of general-anesthesia related to lipid-membrane spontaneous curvature. *Ann. N. Y. Acad. Sci.* **625,** 685–697 CrossRef Medline
82. Kolanjiappan, K., Ramachandran, C. R., and Manoharan, S. (2003) Biochemical changes in tumor tissues of oral cancer patients. *Clin. Biochem.* **36,** 61–65 CrossRef Medline
83. Li, Y. C., Park, M. J., Ye, S. K., Kim, C. W., and Kim, Y. N. (2006) Elevated levels of cholesterol-rich lipid rafts in cancer cells are correlated with apoptosis sensitivity induced by cholesterol-depleting agents. *Am. J. Pathol.* **168,** 1107–1118 CrossRef Medline
84. Pelton, K., Freeman, M. R., and Solomon, K. R. (2012) Cholesterol and prostate cancer. *Curr. Opin. Pharmacol.* **12,** 751–759 CrossRef Medline
85. Chekmenev, E. Y., Jones, S. M., Nikolayeva, Y. N., Vollmar, B. S., Wagner, T. J., Gor'kov, P. L., Brey, W. W., Manion, M. N., Daugherty, K. C., and Cotten, M. (2006) High-field NMR studies of molecular recognition and structure-function relationships in antimicrobial piscidins at the water-lipid bilayer interface. *J. Am. Chem. Soc.* **128,** 5308–5309 CrossRef Medline
86. Gor'kov, P. L., Chekmenev, E. Y., Li, C., Cotten, M., Buffy, J. J., Traaseth, N. J., Veglia, G., and Brey, W. W. (2007) Using Low-E resonators to reduce RF heating in biological samples for static solid-state NMR up to 900 MHz. *J. Magn. Reson.* **185,** 77–93 CrossRef Medline
87. Schwieters, C. D., Kuszewski, J. J., Tjandra, N., and Clore, G. M. (2003) The Xplor-NIH NMR molecular structure determination package. *J. Magn. Reson.* **160,** 65–73 CrossRef Medline
88. Tian, Y., Schwieters, C. D., Opella, S. J., and Marassi, F. M. (2012) AssignFit: a program for simultaneous assignment and structure refinement from solid-state NMR spectra. *J. Magn. Reson.* **214,** 42–50 CrossRef Medline
89. Maciejewski, M. W., Schuyler, A. D., Gryk, M. R., Moraru, I. I., Romero, P. R., Ulrich, E. L., Eghbalnia, H. R., Livny, M., Delaglio, F., and Hoch, J. C. (2017) NMRbox: a resource for biomolecular NMR computation. *Biophys. J.* **112,** 1529–1534 CrossRef Medline
90. Park, S. H., Das, B. B., Casagrande, F., Tian, Y., Nothnagel, H. J., Chu, M., Kiefer, H., Maier, K., De Angelis, A. A., Marassi, F. M., and Opella, S. J. (2012) Structure of the chemokine receptor CXCR1 in phospholipid bilayers. *Nature* **491,** 779–783 CrossRef Medline
91. Tian, Y., Schwieters, C. D., Opella, S. J., and Marassi, F. M. (2014) A practical implicit solvent potential for NMR structure calculation. *J. Magn. Reson.* **243,** 54–64 CrossRef Medline
92. Tian, Y., Schwieters, C. D., Opella, S. J., and Marassi, F. M. (2015) A practical implicit membrane potential for NMR structure calculations of membrane proteins. *Biophys. J.* **109,** 574–585 CrossRef Medline
93. Blaurock, A. E. (1971) Structure of nerve myelin membrane–proof of low-resolution profile. *J. Mol. Biol.* **56,** 35–52 CrossRef Medline
94. Franks, N. P., and Levine, Y. K. (1981) in *Membrane Spectroscopy* (Grell, E., ed), pp. 437–487, Springer-Verlag, Berlin
95. Zhao, J., Wu, J., Heberle, F. A., Mills, T. T., Klawitter, P., Huang, G., Costanza, G., and Feigenson, G. W. (2007) Phase studies of model biomembranes: complex behavior of DSPC/DOPC/cholesterol. *Biochim. Biophys. Acta* **1768,** 2764–2776 CrossRef Medline
96. Konyakhina, T. M., Wu, J., Mastroianni, J. D., Heberle, F. A., and Feigenson, G. W. (2013) Phase diagram of a 4-component lipid mixture: DSPC/DOPC/POPC/chol. *Biochim. Biophys. Acta* **1828,** 2204–2214 CrossRef Medline
97. Levina, N., Tötemeyer, S., Stokes, N. R., Louis, P., Jones, M. A., and Booth, I. R. (1999) Protection of *Escherichia coli* cells against extreme turgor by activation of MscS and MscL mechanosensitive channels: identification of genes required for MscS activity. *EMBO J.* **18,** 1730–1737 CrossRef Medline
98. Edwards, M. D., Black, S., Rasmussen, T., Rasmussen, A., Stokes, N. R., Stephen, T. L., Miller, S., and Booth, I. R. (2012) Characterization of three novel mechanosensitive channel activities in *Escherichia coli*. *Channels* (*Austin*) **6,** 272–281 CrossRef Medline
99. Wiener, M. C., King, G. I., and White, S. H. (1991) Structure of a fluid dioleoylphosphatidylcholine bilayer determined by joint refinement of x-ray and neutron diffraction data. I. Scaling of neutron data and the distribution of double-bonds and water. *Biophys. J.* **60,** 568–576 CrossRef Medline

The host-defense peptide piscidin P1 reorganizes lipid domains in membranes and decreases activation energies in mechanosensitive ion channels

Fatih Comert, Alexander Greenwood, Joseph Maramba, Roderico Acevedo, Laura Lucas, Thulasi Kulasinghe, Leah S. Cairns, Yi Wen, Riqiang Fu, Janet Hammer, Jack Blazyk, Sergei Sukharev, Myriam L. Cotten and Mihaela Mihailescu

J. Biol. Chem. 2019, 294:18557-18570.
doi: 10.1074/jbc.RA119.010232 originally published online October 16, 2019

SUPPORTING INFORMATION

The host-defense peptide piscidin P1 reorganizes lipid domains in membranes and decreases activation energies in mechanosensitive ion channels

Fatih Comert[1], Alexander Greenwood[2], Joseph Maramba[3], Roderico Acevedo[1], Laura Lucas[4], Thulasi Kulasinghe[1], Leah Cairns[5], Yi Wen[6], Janet Hammer[7], Jack Blazyk[7], Sergei Sukharev[3], Myriam L. Cotten[5] and Mihaela Mihailescu[1*]

Table of Contents

TABLE S1. EC_{50} values for the permeabilization effects of P1 and P3 on different membrane systems.

EC_{50} (P/L)	**P1**	**P3**
POPC	1:166	1:28
4:1 POPC/Chol	1:130	1:23
1:1 POPE/POPG[a]	1:10	1:3
3:1 POPC/POPG[b]	1:22	1:4

[a] From Hayden et al. (1). [b]From Mihailescu et al. (2).

TABLE S2. Structure factors (f) and standard deviation (sd) of all observed Bragg diffraction peaks for oriented DiPoPE multilayers. Δf are differences between structure factors of the same sample measured in ^2H_2O versus H_2O.

h	**f**	**sd**	**Δfw20**[a]	**sd**	**Δfw50**[b]	**sd**
1.00	-5.72	0.00	-5.50	0.01	-13.74	0.01
2.00	-3.15	0.01	3.21	0.02	8.03	0.01
3.00	2.90	0.01	-1.07	0.01	-2.67	0.04
4.00	-2.33	0.01	0.23	0.01	0.58	0.01
5.00	0.61	0.03	-0.05	0.04	-0.13	0.04
6.00	0.00	0.06	0.00	0.08	0.00	0.09

[a-b] For measurements in 20:80 ^2H_2O: H_2O and 50:50 ^2H_2O: H_2O.

TABLE S3. Structure factors (f) and standard deviation (sd) of all observed Bragg diffraction peaks for oriented DiPoPE multilayers with P1. Δf are differences between structure factors of labeled versus unlabeled homologous samples.

h	**f**	**sd**	**Δfw20**[a]	**sd**	**Δfw50**[b]	**sd**	**Δfd33**[c]	**sd**
1.00	-6.40	0.01	-5.76	0.01	-14.85	0.01	-1.77	0.02
2.00	-3.39	0.01	2.91	0.02	7.02	0.01	0.06	0.01
3.00	2.74	0.01	-0.83	0.02	-1.87	0.02	0.72	0.01
4.00	-1.34	0.02	0.10	0.03	0.14	0.03	-0.51	0.01
5.00	0.00	0.09	0.00	0.11	0.00	0.11	0.31	0.02

[a-b] Same as in Table S2. [c]For measurements using deuterated peptide.

TABLE S4. RMSDs and number of restraints for structures of P1 and P3. Restraints are defined as either dihedral angles (phi/psi), dipolar couplings (DC), or anisotropic chemical shifts (CSA). RMSDs were determined for the α-helical region that does not experience fraying (residues 3-20) of the top ten structures and are given in Å.

	DC restraints	CSA restraints	phi/psi torsion restraints	heavy-atom RMSD	alpha-carbon RMSD	all-atom RMSD	violations/structure
P1 in PC/Chol	20	21	40	1.16	0.36	1.44	0.2
P3 in PC/Chol	20	20	40	1.12	0.19	1.39	0

TABLE S5. Tilt (τ) and rotation (ρ) angles of P1 and P3. Separate values are shown for the N-terminal (residues 3-10) and C-terminal (residues 14-20) ends of the peptides.

	3-10		14-20	
	τ	ρ	τ	P
P1 in PE/PG[1]	83 ± 3	253 ± 2	86 ± 1	218 ± 2
P1 in PC/Chol	85 ± 1	248 ± 1	80 ± 1	211 ± 2
P3 in PE/PG[1]	92 ± 1	250 ± 2	83 ± 2	220 ± 2
P3 in PC/Chol	85 ± 1	237 ± 1	83 ± 1	212 ± 2

TABLE S6. Projected areas of P1 and P3 in POPC/cholesterol and POPE/POPG. The projected areas (in units of Å^2) of P1 and P3 are given for the projections onto two planes: the plane of the bilayer (xy), and the plane parallel to the helical axis and perpendicular to the bilayer (xz).

	bilayer plane "xy"	"xz"
P1 in PE/PG[1]	439.3	465.0
P1 in PC/Chol	435.1	511.2
P3 in PE/PG[1]	429.5	480.5
P3 in PC/Chol	432.8	487.2

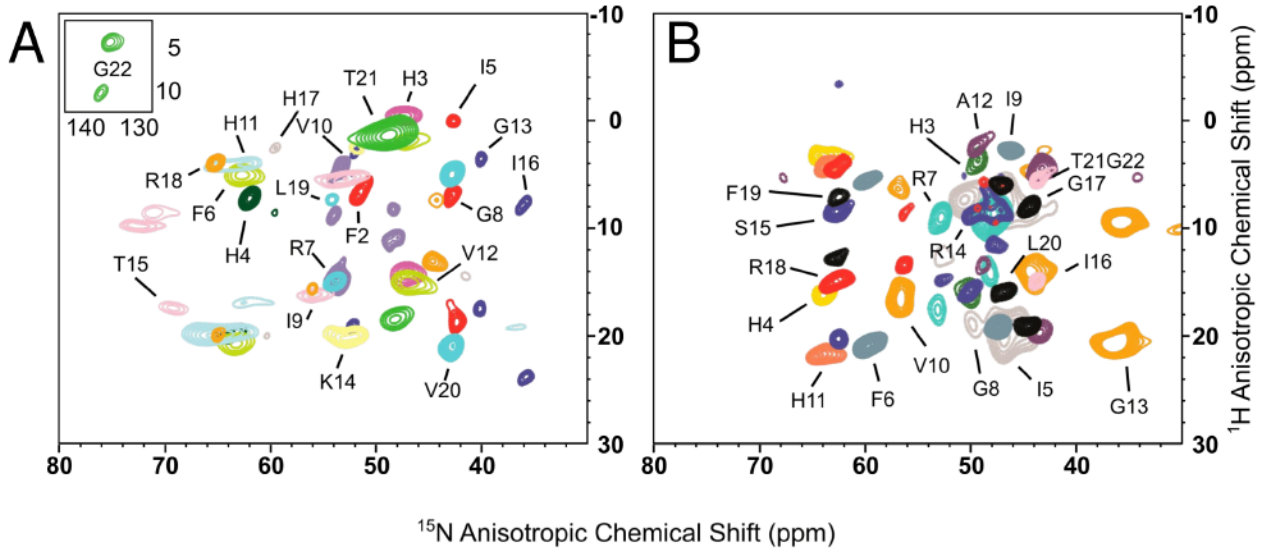

Figure S1. **Solid-state NMR spectra for P1 and P3 in POPC/cholesterol.** *A*, The HETCOR spectra for several multiply-labeled P1 samples, in aligned 4:1 POPC/Chol fluid bilayers. *B*, Same as in *A*, for P3. The spectra were collected at 32 °C and P/L = 1:40. The individual spectra, which are stacked here, were collected for the bilayer normal parallel to the static magnetic field. Each ^{15}N-labeled site gives rise to a splitting in the ^{1}H dimension due to the ^{15}N-^{1}H dipolar couplings. Both the ^{15}N chemical shift and ^{15}N-^{1}H dipolar coupling of a given ^{15}N-labeled amide site are used for the structural determination (see methods and (3) for more details).

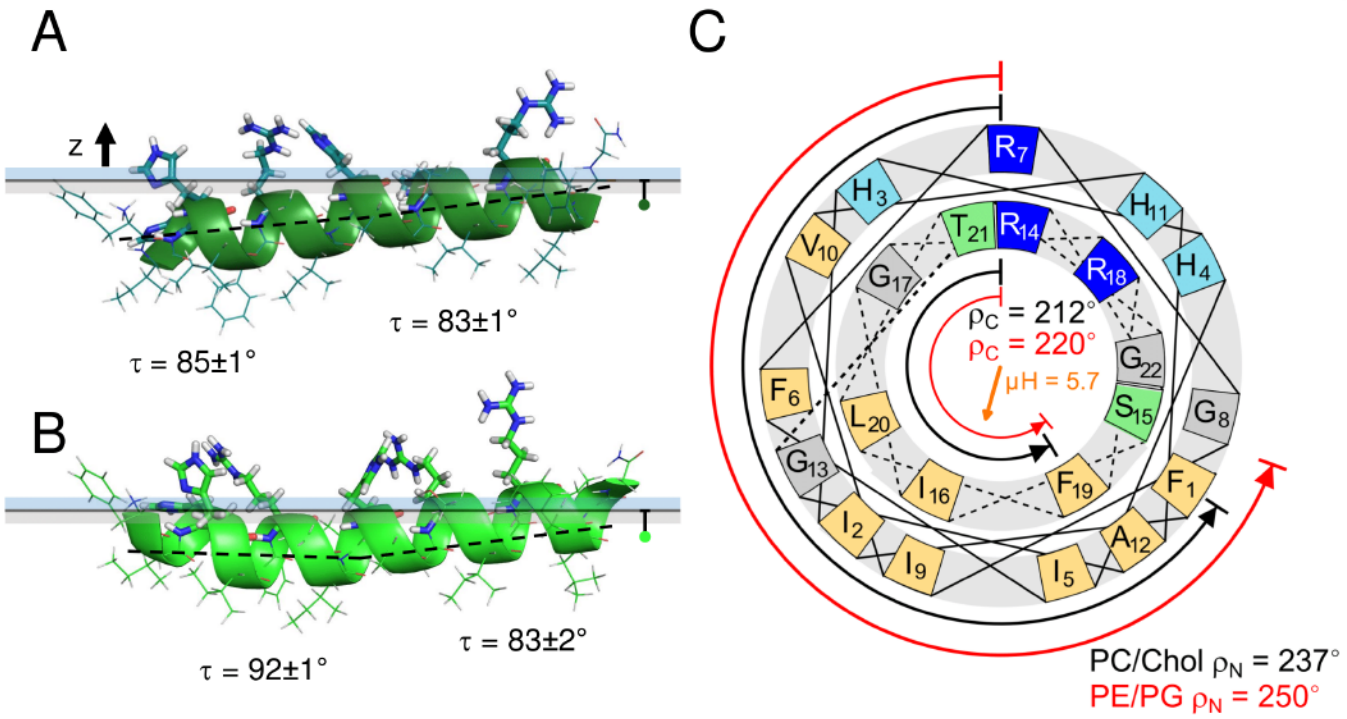

Figure S2. **NMR structures of P3 bound to POPC/Chol oriented multilayers.** *A,* Structure of P3 bound to 4:1 POPC/Chol fluid bilayers, studied at 32 °C (PDB ID #6PEZ). The NMR samples were prepared at pH 7.4 and using a P/L of 1:40. The structure, which represents the lowest-energy member of the ensemble of structural conformers, is displayed for a peptide partitioned in the upper leaflet of the bilayer. Hence, basic (stick representation) and hydrophobic side chains pointing upward and downwards, respectively. Grey lines represent the average position of the C2 atoms of the lipids, based on prior molecular dynamics determination (4), and green dots are shown to represent the position of the peptide center of mass. The RMSD between the top ten structures is 1.12 Å in the α-helical region that experiences no fraying (residues 3-20) (see Supplementary Table S4). *B,* Structure of P3 previously solved in 1:1 POPE/POPG (PDB ID # 2MCX) (3). *C*, Helical wheel diagram of P3 in 4:1 POPC/Chol. The angle ρ refers to the rotation of the α-helix with respect to its axis, and relate to the ability of the peptide to rotate and place its hydrophobic side chains in the hydrocarbon core of the bilayer (3). Because the peptide is kinked at a central glycine, Gly13, the ρ values are different for the N- and C-terminal regions, as indicated by different ρ_N and ρ_C values respectively. Red arrows and values represent the rotation angles for P3 in POPE/POPG for comparison, and the orange arrow represents the direction of the hydrophobic moment.

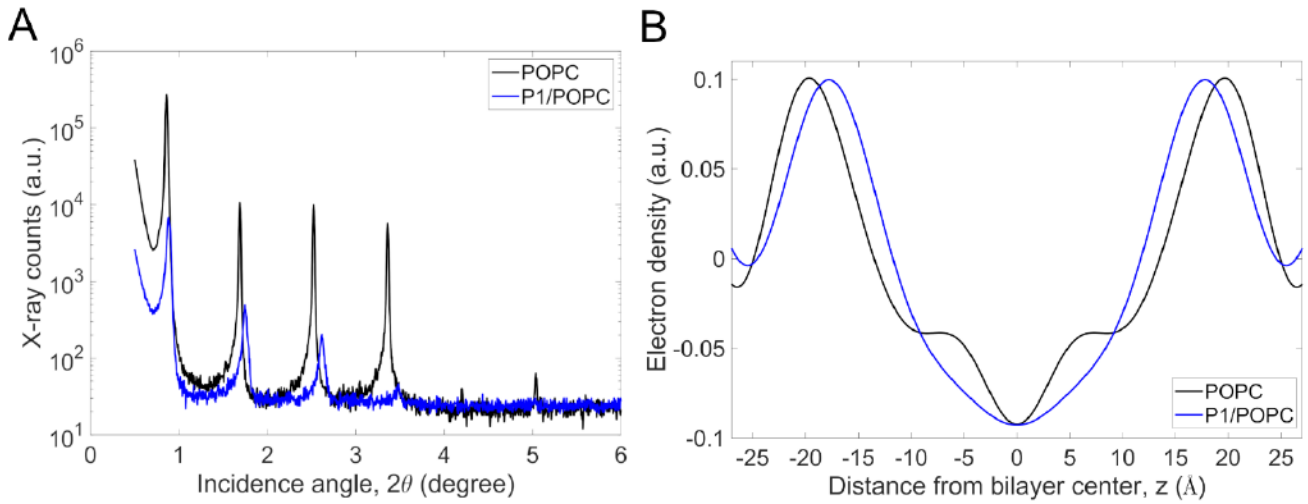

FIGURE S3. **X-ray diffraction data for oriented multilayer samples of POPC and P1/POPC**. *A,* control samples of POPC (black) and P1/POPC, at P/L = 1:25 molar ratio. The repeat spacings are 53.0 Å (0.04) for POPC and 51.0 Å (0.1) for P1/POPC. *B,* bilayer profiles calculated from the data in *A*. Note the migration of the lipid headgroup toward the bilayer interior (blue) compared to pure lipid (black).

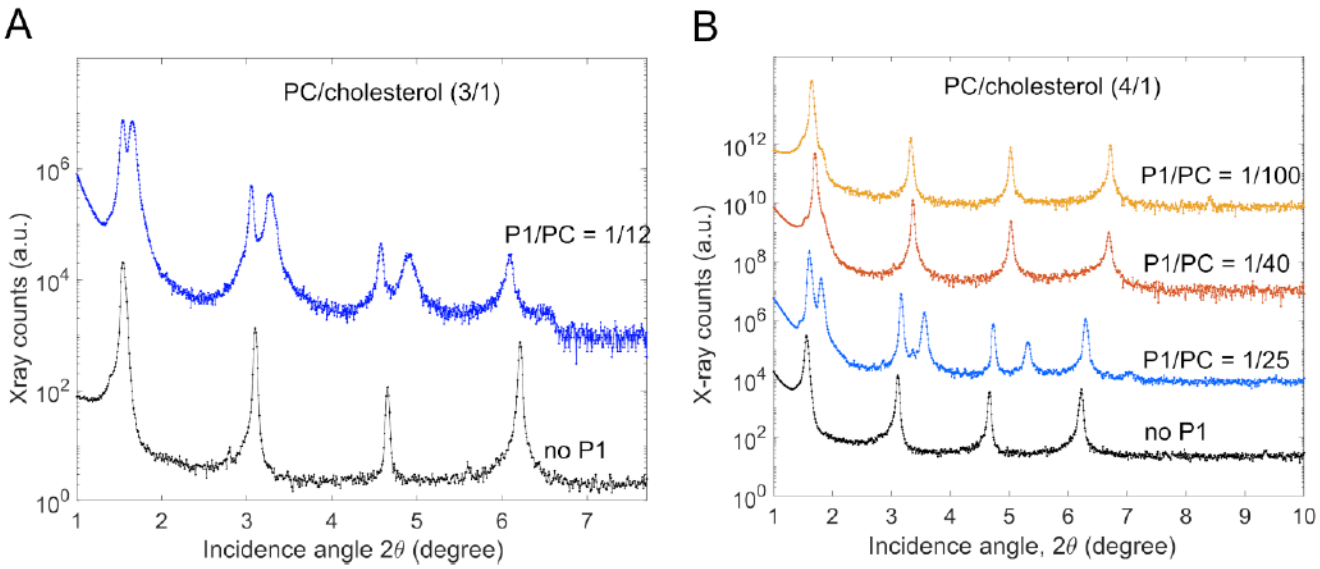

FIGURE S4. **X-ray diffraction data for oriented multilayer samples of P1 in POPC/cholesterol.** *A,* POPC/cholesterol (1:0.33) without peptide (black) and P1/POPC/cholesterol (0.08:1:0.33) (blue). The peptides and lipids we mixed in organic solvent, prior to forming liposomes in water and aligned multilayers. *B,* POPC/cholesterol (1:0.25) without peptide (black), P1/POPC/cholesterol = 0.04:1:0.25 (blue), P1/POPC/cholesterol = 0.025:1:0.25 (red) and P1/POPC/cholesterol = 0.01:1:0.25. The peptide was added to preformed POPC/cholesterol liposomes in water. All data sets were measured at 98% relative humidity and 25 °C, unless otherwise specified.

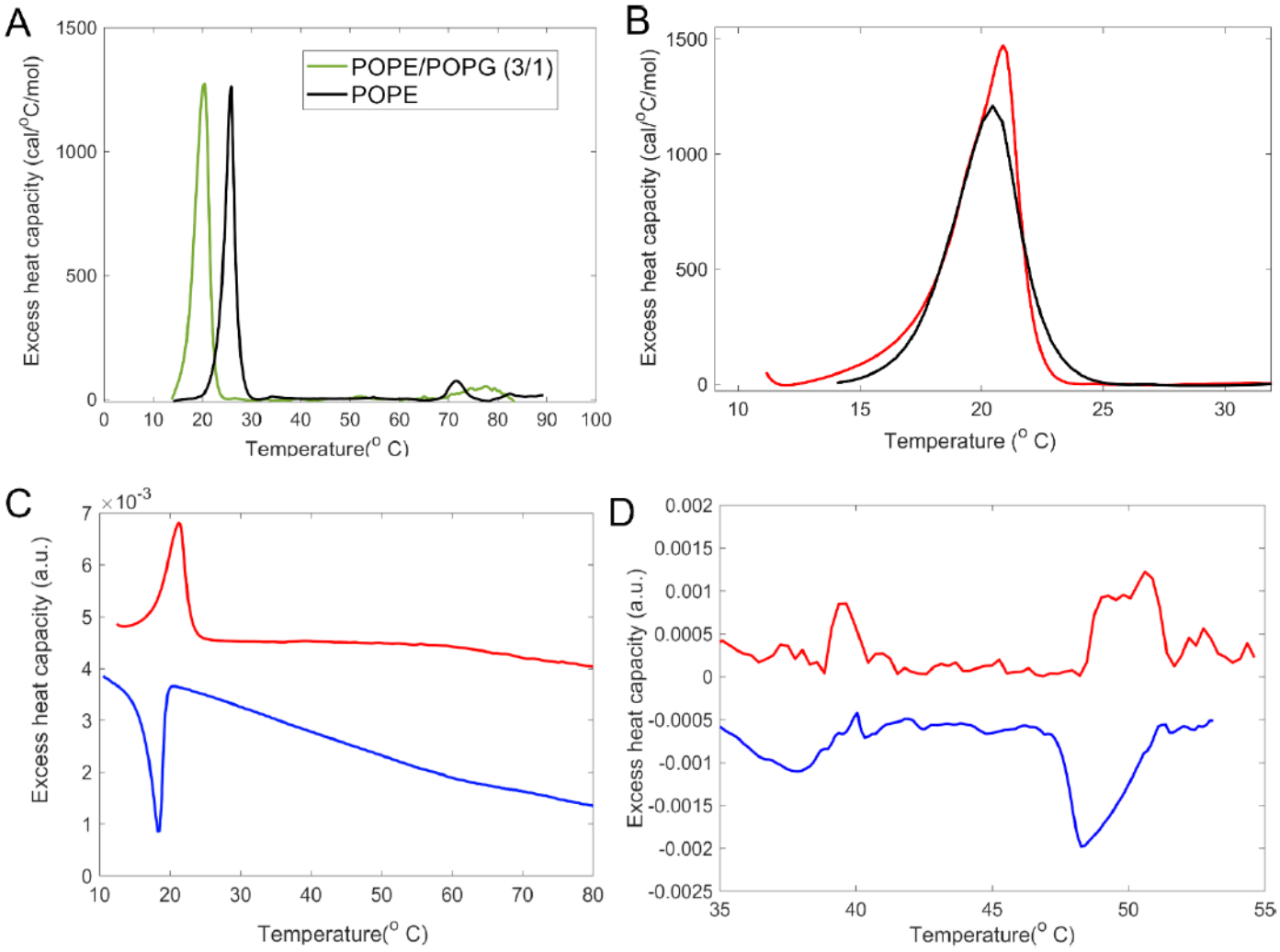

FIGURE S5. **Differential Scanning Calorimetry in POPE/POPG mixtures.** *A,* Heating scan of POPE and POPE/POPG (3:1 molar ratio) showing the main melting transition at 25 and 20 degrees Celsius (° C), respectively. The lamellar to inverted hexagonal transition for POPE is seen at 72 ° C. *B,* Heating scans for the melting transition of POPE/POPG (3:1) (black) and P3/POPE/POPG, at P/L = 1:50 (red). Peak maxima are at 20.5 ° and 20.9 ° C, respectively. *C,* Raw heating (red) and cooling (blue) scans for P1 in POPE/POPG, P/L= 1:50. The curves were shifted for better visibility. *D,* Raw, heating (red) and cooling (blue) scans for P1 in diPoPE, P/L= 1:350. All samples were prepared in water except for sample in *D*, which was prepared at 2.5 milligrams per milliliter in 10 mmol/L PIPES, 50 mmol/L NaCl, 0.5 mmol/L EDTA, pH 7.4. Scan rates were at 0.5 degrees per minute.

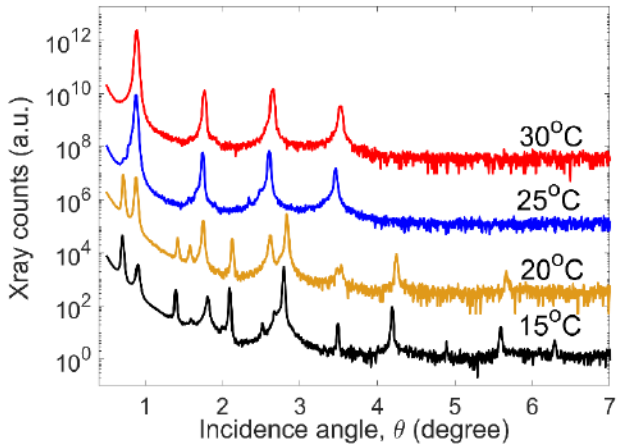

FIGURE S6. **Lamellar X-ray diffraction data for POPE/POPG with P3.** The peptide was incorporated in POPC/POPG (3:1) at P/L = 1:25, molar ratio. Measurements were performed at 98% relative humidity, allowing the sample to equilibrate for 1 hour after each temperature change.

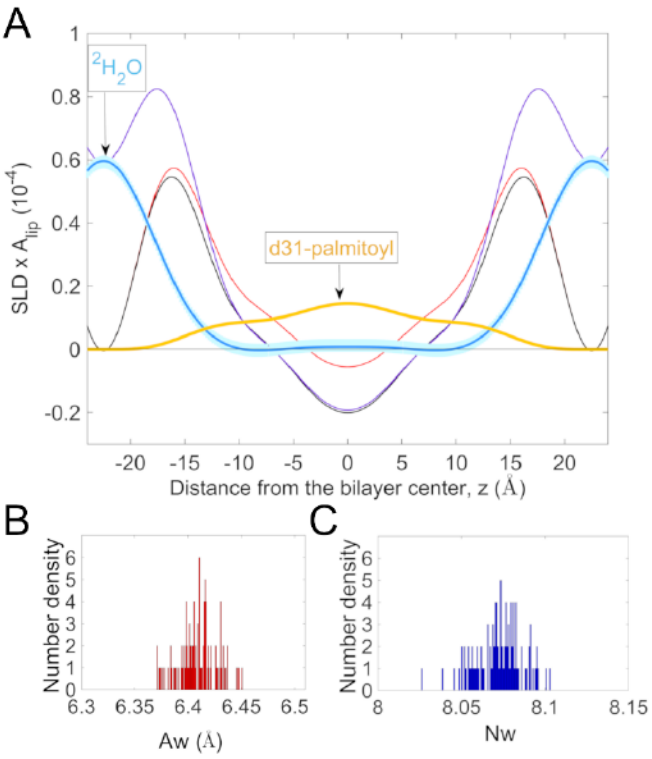

FIGURE S7. **Calibration of water content in diPoPE bilayers, with deuterium labeling.** *A,* Calibrated neutron scattering length density (SLD) profiles of a bilayer made of DiPoPE with 5% POPG, measured in H_2O (black), superposed over the profiles containing ^2H-labeled homologs: unlabeled bilayer measured in ^2H_2O (purple), and bilayer containing labeled lipid chain (d31-POPG) measured in H_2O (red). Measurements were done at 93% relative humidity and 23 ° C. Deuterium difference results in the d31-palmitoyl profile (yellow) and water (blue). The deuterium profiles are shown with uncertainty bands. The amount of deuterium in the chain (d31) is used as a means for calibration of SLD profile amplitudes and for determining the amount of water in the bilayer, based on known lipid composition. *B-C,* statistic for determining water distribution parameters: 1/e-halfwidth (Aw) and number of water per headgroup (Nw). The water content was calculated to be 8.08 (0.04) per lipid headgroup.

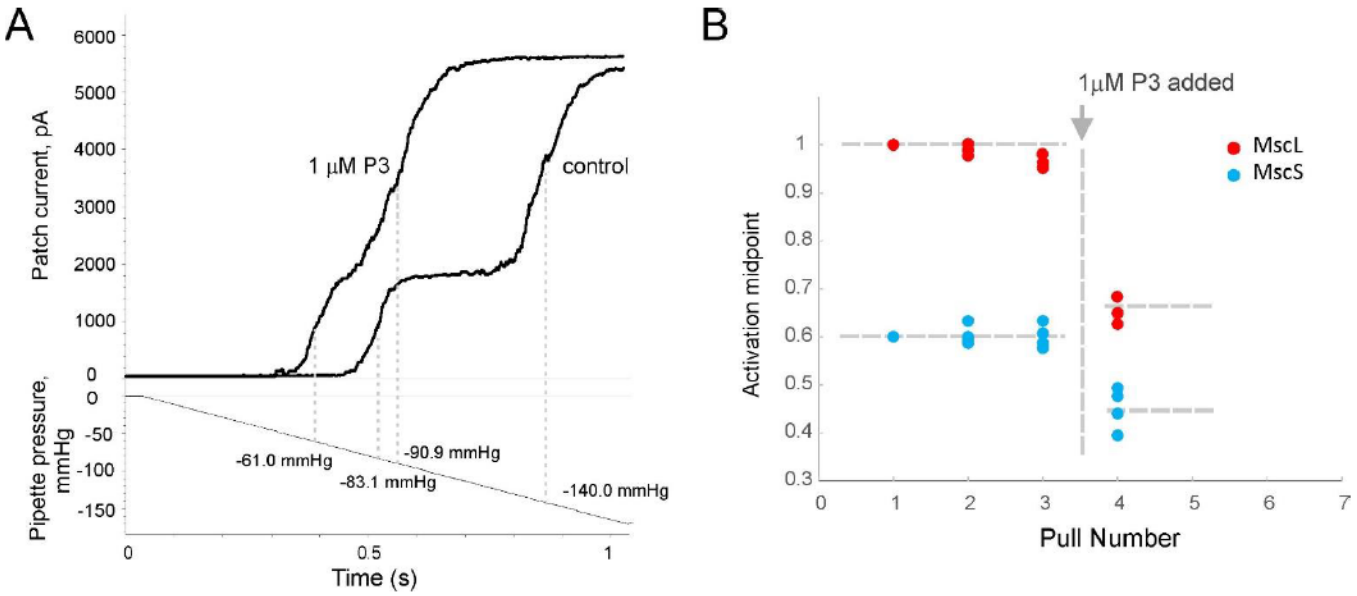

FIGURE S8. **Effects of Piscidin 3 on activation midpoints of mechanosensitive channels MscS and MscL in the native inner membrane of *E. coli*.** Measurements were done in isolated inside-out patches excised from giant spheroplasts at +30 mV pipette voltage. (Recording buffer: 200 mmol/L KCl, 90 mmol/L $MgCl_2$, 10 mmol/L $CaCl_2$, 5 mmol/L HEPES). Each patch was tested with identical linear ramps (pulls) of pressure. Three ramps were applied sequentially with 5 min intervals to make sure that the naïve patch is stable. Then 1.0 μM of P3 was introduced to the cytoplasmic side of the patch. After a 15 min equilibration period the fourth ramp was applied and the midpoint shifts compared to pull 3 were scored. *A,* Two-wave current responses reflect activation of MscS population first, followed by a wave of MscL activation. *B,* Cumulative data obtained on 4 independent patches illustrating a substantial decrease of activating (midpoint) pressure for both channels by P3. For MscS, the relative midpoint shifted from 0.60±0.02 to 0.45±0.04, (n=4) whereas for MscL the midpoint shifted from 0.97±0.002 to 0.66±0.03 (n=3). The midpoint values are normalized to the activation midpoint of MscL in controls. None of the patches survived the fifth ramp. Concentrations of P3 higher than 1.0 μmol/L strongly destabilized the patches precluding the measurements. See main text.

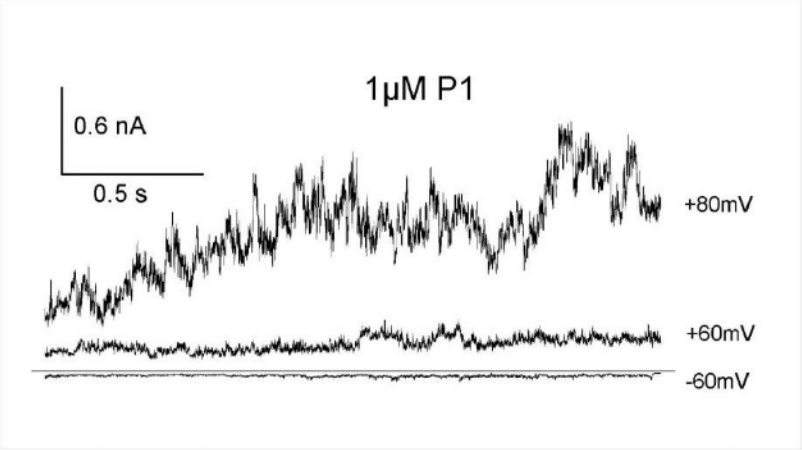

FIGURE S9. **Current fluctuations at high voltages in patches treated with P1.** Piscidin 1 present at 1 μmol/L concentration on the cytoplasmic surface of the inside-out patch excised from the inner *E. coli* membrane produces a fluctuating conductance at elevated hyperpolarizing voltages (+60 or 80 mV in the pipette). We do not observe such fluctuations at voltages below 50 mV.

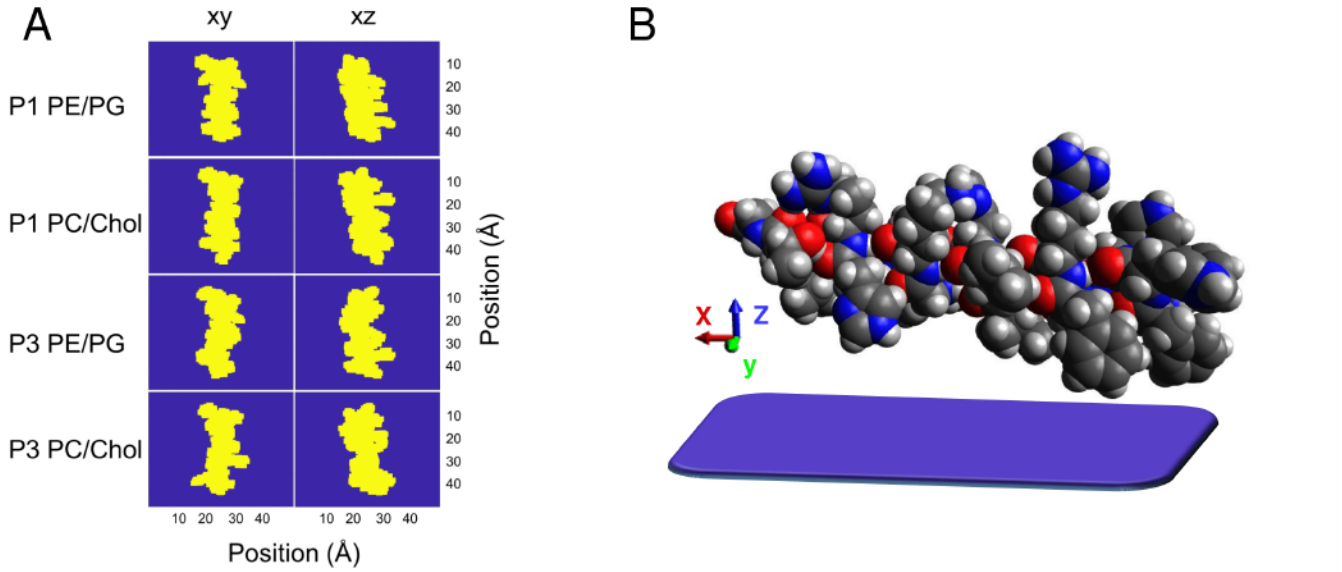

Figure S10. **Projected areas of P1 and P3 in POPC/cholesterol and POPE/POPG.** *A*, The projections of P1 and P3 onto two planes: the plane of the bilayer (xy), and the plane parallel to the α-helical axis and perpendicular to the bilayer (xz). *B*, Schematic showing the three axes relative to the structure of P1 in PC/Chol. The plane of the bilayer (xy) is shown in blue below the peptide.

References

1. Hayden, R. M., Goldberg, G. K., Ferguson, B. M., Schoeneck, M. W., Libardo, M. D. J., Mayeux, S. E., Shrestha, A., Bogardus, K. A., Hammer, J., Pryshchep, S., Lehman, H. K., McCormick, M. L., Blazyk, J., Angeles-Boza, A. M., Fu, R. Q., and Cotten, M. L. (2015) Complementary Effects of Host Defense Peptides Piscidin 1 and Piscidin 3 on DNA and Lipid Membranes: Biophysical Insights into Contrasting Biological Activities. *J. Phys. Chem. B* **119**, 15235-15246
2. Mihailescu, M., Sorci, M., Seckute, J., Silin, V. I., Hammer, J., Perrin, B. S., Hernandez, J. I., Smajic, N., Shrestha, A., Bogardus, K. A., Greenwood, A. I., Fu, R. Q., Blazyk, J., Pastor, R. W., Nicholson, L. K., Belfort, G., and Cotten, M. L. (2019) Structure and Function in Antimicrobial Piscidins: Histidine Position, Directionality of Membrane Insertion, and pH-Dependent Permeabilization. *J. Am. Chem. Soc.* **141**, 9837-9853
3. Perrin, B. S., Jr., Tian, Y., Fu, R., Grant, C. V., Chekmenev, E. Y., Wieczorek, W. E., Dao, A. E., Hayden, R. M., Burzynski, C. M., Venable, R. M., Sharma, M., Opella, S. J., Pastor, R. W., and Cotten, M. L. (2014) High-resolution structures and orientations of antimicrobial peptides piscidin 1 and piscidin 3 in fluid bilayers reveal tilting, kinking, and bilayer immersion. *J. Am. Chem. Soc.* **136**, 3491-3504
4. Perrin, B. S., Jr., Sodt, A. J., Cotten, M. L., and Pastor, R. W. (2015) The Curvature Induction of Surface-Bound Antimicrobial Peptides Piscidin 1 and Piscidin 3 Varies with Lipid Chain Length. *J. Membr. Biol.* **248**, 455-467